Aerodynamic Shape Optimization of a Blended-Wing-Body Aircraft Configuration

by

Nimeesha B. Kuntawala

A thesis submitted in conformity with the requirements
for the degree of Masters of Applied Science
Graduate Department of Aerospace Engineering
University of Toronto

Abstract

Aerodynamic Shape Optimization of a Blended-Wing-Body Aircraft Configuration

Nimeesha B. Kuntawala

Masters of Applied Science

Graduate Department of Aerospace Engineering

University of Toronto

2011

Increasing environmental concerns and fuel prices motivate the study of alternative, unconventional aircraft configurations. One such example is the blended-wing-body configuration, which has been shown to have several advantages over the conventional tube-and-wing aircraft configuration. In this thesis, a blended-wing-body aircraft is studied and optimized aerodynamically using a high-fidelity Euler-based flow solver, integrated geometry parameterization and mesh movement, adjoint-based gradient evaluation, and a sequential quadratic programming algorithm. Specifically, the aircraft is optimized at transonic conditions to minimize the sum of induced and wave drag. These optimizations are carried out with both fixed and varying airfoil sections. With varying airfoil sections and increased freedom, up to 52% drag reduction relative to the baseline geometry was achieved: at the target C_L of 0.357, a C_D of 0.01313 and an inviscid lift-to-drag ratio of 27.2 were obtained.

Acknowledgements

I would like to thank Prof. David W. Zingg for giving me the opportunity to work as part of his group on this exciting project, which has been motivational in itself. It has been an honour to learn from and work with him over the years. I have learned not only the fundamentals of aerodynamics and good research from him, but also what makes an excellent supervisor and a great leader. Thank you for all your help, guidance, encouragement, and patience.

I would also like to thank my committee members: Prof. Joaquim R. R. A Martins for always being willing and ready to answer my questions and for his enthusiasm for my project, and Profs. Phillipe Lavoie and Alis Ekmekci for their insightful questions and thoughts.

My experience at UTIAS has been made all the more pleasant by the administrative staff: Joan, Clara, Gail, Jeff, Nora, Peter, and Rosanna — thank you.

I also owe thanks to members of the CFD group: specifically, I am very grateful to Dr. Jason E. Hicken for all his help over the course of my thesis. I would also like to thank Lana and Michal Osusky, Dr. Timothy Leung, Howard Buckley, Hugo Gagnon, and Oleg Chernukhin for the tips and interesting discussions. Being a part of this group and working alongside such a talented group of people has been inspiring and has pushed me to raise the bar for myself.

For his computational solutions, I am very grateful to Scott Northrup. Thanks also to Gaetan Kenway, Sandy Mader, and Graeme Kennedy from the MDO group for sharing their expertise.

To my friends: thank you for your friendship, support, encouragement and most importantly, the laughs, the breaks, and the memories.

To my family: Prateesha and Reena — thank you for your love, for always believing in me, and for teaching me what the textbooks could not; my parents — thank you for your endless love, support, encouragement, and for working so hard to put opportunities such as this within reach. Your perseverance and determination to do so continue to inspire me everyday.

Nimeesha B. Kuntawala

University of Toronto Institute for Aerospace Studies
June 12, 2011

Contents

List of Tables

List of Figures

Chapter 1

Introduction

1.1 Motivation

1.1.1 The Need for Change

> *How could the desire for a modern way of life that threatens our future be considered a **way** of life? Could it be we are connected to all things in the universe?...That suburbs in Los Angeles affect the melting ice caps of Antarctica? Deforestation in the Congo affects the typhoons of Japan? Now we must face the insurmountable challenges for what they really are: opportunities to reinvent and redesign.*
>
> - e^2 Series [49]

Climate change is clearly a global problem, with potentially dire effects. As of 2008, the atmospheric concentration of greenhouse gases was approximately 430ppm CO_2eq[1], and the minimum, inevitable global temperature rise was predicted to be 2.5°F [77]. But what if the temperature rise is higher? Assuming a greenhouse gas stabilization at 450ppm CO_2eq, the temperature rise would likely be between 3.5 and 6.5°F with the most probable rise being approximately 4.5°F. Some of the more threatening effects of such

[1] **carbon dioxide equivalent** defined as the measure of the combined effects of all greenhouse gases including carbon dioxide, methane, nitrogen oxide, and other trace greenhouse gases (e.g. chlorofluorocarbons) [77]

rises include: increased heat waves, droughts, and fires in continental areas, increase in intensity of hurricanes and rainfall causing potential flooding at warming of up to 3.5°F. Adding to these effects, for warming in the 3.5 to 5.4°F range, 20 to 30% of all species on Earth are at increasingly high risk of extinction. In addition to victims of an increase to 3.5°F, up to 10 million more people are at risk of hunger and up to 3 million more at risk of flooding. For a 5.4 to 7.2°F range, an eventual sea-level rise of forty feet due to the increasing probability of almost complete melting of Greenland and West Antarctic ice sheets and reduced global food production are just two of the many potential effects. Higher greenhouse gas stabilization goals means higher ranges of temperature changes and even worse effects [77].

Indeed, increasing environmental concerns are a global issue faced by many industries, and the aerospace industry is no exception. While aviation is responsible for about 4.9% of global greenhouse emissions [27], growth in the industry is only expected to increase. For instance, between 2009 and 2029, Boeing predicts an annual growth of 5.3% in total world traffic flow [68]. Aviation is a culprit for more than just the expected growth [77]: first, planes are delivering nitrogen oxides at higher altitudes and therefore, very efficiently contributing to the problem. Combined with the effects of cirrus clouds from contrails, the direct effect of carbon dioxide is tripled [65, 77]! Secondly, since not everyone is flying or can even afford to fly, an inequality in responsibility exists. Finally, immediate alternatives to fossil fuels are not quite available: hydrogen could add to cirrus clouds; biofuels are promising but unlikely to replace standard jet fuel for several decades, leaving fuel efficiency improvement as one of the key options [77]. Improving fuel efficiency is not only important from an environmental perspective, but also from an economics perspective: with increasing fuel prices — up by almost 13% from about a year ago [22] — airlines will need more fuel efficient options given the predicted growth in the air traffic.

The work in this thesis brings two ideas together — the unconventional blended-wing-

body aircraft configuration and high-fidelity aerodynamic shape optimization — in the hopes of effectively contributing to the development of future solutions which are more fuel-efficient and environmentally-friendly.

1.1.2 The Blended-Wing-Body

The blended-wing-body (BWB) aircraft configuration is an alternative configuration which eliminates the tail on the conventional aircraft and blends the fuselage with the wing. Essentially, it is a flying wing. As noted by Liebeck *et al.* [52], Kroo [25], Siouris and Qin [63] and other researchers, while significant improvements in efficiency have been achieved over the past few decades with the existing conventional aircraft configuration — through aerodynamic performance, advanced composites, flight control system, and engine fuel efficiency improvements — the overall configuration has changed very little. These changes can be considered more evolutionary than revolutionary. Evolutionary changes, for the most part, maintain the existing tube-and-wing aircraft configuration while tweaking the shape and incorporating different technologies such as improved structural materials in order to increase the efficiency of the aircraft as a whole. The BWB configuration, on the other hand, is a revolutionary change in aircraft configuration [26, 52]. Analogous examples include the joined wing and oblique flying wing aircraft configurations. These unconventional aircraft present potential benefits over the tube-and-wing configuration which might otherwise be impossible to achieve. Consequently, they may ultimately help to more effectively target the environmental issues and fuel efficiency concerns being faced by our industry.

Specifically, the BWB configuration is a promising alternative to the existing configuration. Liebeck [29] showed that a BWB designed for approximately 800 passengers and a range of 7000 nautical miles results in a 27% reduction in fuel consumption per passenger-km compared to a conventional aircraft configuration. These and further studies, along with a discussion of the advantages and disadvantages of the BWB, will be

outlined in Section 1.2.

1.1.3 High-Fidelity Simulation and Optimization Tools

As pointed out by Kroo [25], higher fidelity optimization used at a conceptual design phase could lead to new and innovative shapes, which might not have been discovered otherwise. Several aspects of work done by Hicken and Zingg [18, 21, 19, 20] have the ultimate goal of answering the questions of if and how numerical optimization can be employed in the discovery of novel aerodynamic components or configurations. For instance, one such tool is an integrated geometry parameterization and mesh movement which provides a flexible parameterization linked with a robust and rapid mesh movement algorithm [20]. Details of this and other aspects of the tools used for this purpose, such as the flow solver, gradient evaluation and optimizer, will be discussed in Chapter 4 of this thesis. Results of work by Hicken [18] also demonstrate the potential for 'discovering' aerodynamically efficient features: through an Euler based optimization, an initially flat plate was optimized to include winglets which resulted in an 8% induced drag reduction. In similar manner, we might learn of new features or shapes specifically for a BWB-type aircraft.

1.2 Background

1.2.1 Advantages of the Blended-Wing-Body

Several features of the BWB configuration contribute to its increase in fuel efficiency. These features, along with additional advantages of the BWB configuration, are discussed here. While some of these advantages might be specific to a given study, they are included as an illustration of the potential for this advantage over a conventional configuration.

Aerodynamics

A key aspect of the BWB is its lift-generating centerbody — a gain over the cylindrical fuselage of a conventional aircraft — which improves the aerodynamic performance by reducing the wing loading [46, 48, 63]. In addition, the decrease in wetted area, via a smaller outer wing, relative to a similar sized conventional aircraft translates into an increased lift-to-drag ratio, since it is proportional to the wetted aspect ratio; this aspect ratio increases due to its inverse proportionality to the wetted area [29, 31, 59, 53]. The lower wetted area to volume ratio for larger BWBs in comparison to conventional aircraft also adds to the benefit. Interference drag is reduced due to the elimination and reduction of junctions which exist between the wings and fuselage on conventional aircraft [55, 53, 54, 63, 50, 46], resulting in a more streamlined shape for the BWB. The absence of the horizontal tail also implies a reduction in the corresponding friction and induced drag penalties, further increasing the lift-to-drag ratio [1].

The naturally area-ruled shape of the BWB means higher cruise Mach numbers are more easily attainable without changes in the basic configuration geometry [60, 29]. In fact, the BWB's cross-sectional area variation resembles that of the body of minimum wave drag due to volume, the Sears-Haack body, translating into wave drag reductions at transonic speeds [60, 29].

With engines partially embedded in the BWB aft-body, an advantage unique to this configuration arises: the potential for boundary layer ingestion from a portion of the centerbody upstream of the engine inlet. Not only does this aft-location of the engines effectively balance the airframe and offset the weight of the payload, furnishings, and systems, but it also ensures that such Boundary Layer Ingestion (BLI) technology has greatest effect since the boundary layer is fully developed towards the rear of the wing [8]. In addition, through the reduction of ram drag, this BLI technology can provide improved propulsive efficiency [31, 29], as well as reductions in required thrust and fuel burn [8]. Finally, the potential for further drag reduction through passive and active laminar flow

control via wing shaping and laminar flow technology on the engine nacelle and lifting surfaces is present, as the BWB configuration is well-suited for such technologies. This would imply potentially substantial reductions in skin friction drag [53].

Aero-structures

Since the lift-generating fuselage extends spanwise, the lift and payload are much more in line with each other on the BWB than on a conventional aircraft [50]. Essentially, the passenger cabin is used as a wing bending structure. Consequently, the cantilever span of the thin outer wing is reduced, and the BWB weight is distributed more optimally along the span [31]. This integration of the thick centerbody with the outer wing translates into reduced bending moments and thus reduced structural weight [53, 50, 63]. For the Boeing configuration presented by Liebeck [31], this effect resulted in peak bending moment and shear on the BWB which were half that of a conventional configuration. As mentioned above, this integration also reduces the total wetted area and allows for a long wingspan [52, 31]. As a result, the optimal aspect ratio of the outer wing can be slightly greater than that for conventional wings [1]. Thus, not only does the wing have a higher lift-to-drag ratio, but it is also structurally efficient [52, 31, 1].

Noise Reduction

Even prior to the implementation of specific acoustic treatments, the BWB configuration has a low acoustic signature [29]. For this reason, the BWB was selected for the MIT/Cambridge Silent Aircraft Initiative project (SAI), which had the goal of designing an aircraft with reduced noise [8]. The airframe has no tail, smooth lifting surfaces and minimally exposed edges and cavities, contributing to its low-noise nature. The BWB is more of a noise-shielded configuration than current conventional aircraft on which the engines hang below the wing [8]. In the case where engines are located on the aft-body of the BWB [52, 8, 63], the inlets are hidden from below by the centerbody, which also

serves as a shield for forward radiated fan noise. Furthermore, engine exhaust noise is not reflected from the under surface of the wing, benefiting both the passengers and areas surrounding airports [31, 29, 1]. Due to more specific features of the Boeing design, airframe noise is further reduced through the absence of slotted flaps — due to the low wing loading — for the trailing edge high-lift system and all the mechanisms which support them [31, 29].

Marketing And Manufacturing

In terms of passenger comfort levels in the BWB, this configuration's vertical cabin walls might present a more spacious environment than the current curved walls of conventional aircraft [29]. Liebeck [29] compares this design and spacious environment to that in a railroad car. Direct operating costs per seat/mile for the BWB are also estimated to be 15% lower than current conventional designs [1]. Due to the simplicity of the BWB configuration, such as the elimination of fillets and joints of highly loaded structures at 90 degrees to each other, a significant reduction in the number of parts — on the order of 30% — has also been estimated [30, 29]. A two-fold sense of commonality is another design constraint considered by the Boeing team [30] as a result of the BWB's unique capability to be stretched and re-configured:

Size: commonality between different sizes of the BWB in order to create a family of aircraft

Application: commonality between military and commercial applications.

For the former, the aircraft can be stretched laterally, enabling the addition of span and wing area while increasing the payload. This advantageous capability is not afforded by conventional aircraft which are longitudinally stretched to increase payload [29]. Specifically, commonality between 250-passenger and 450-passenger versions has been studied, with the outer wings and nose/cockpit section being common between members of

this aircraft family. The necessary fuel volume in the outer wing is adequate for all members of the family, and the modular centerbodies are aerodynamically smooth and balanced. Furthermore, such commonality offers 23% reduction in non-recurring costs and 12% reduction in recurring costs compared to the stand-alone cases for the 250- and 450-passenger versions. Such cost reduction would likely increase with the inclusion of additional sizes of BWB, such as a 350-passenger version [30, 29]. For the Boeing cabin design, this commonality between families also extends to the interior with the growth concept in place, since the cabin cross-sections would be the same between the different aircraft. For airlines, these benefits mean fleet mix requirements can be easily accommodated, manufacturing learning curve penalties are reduced, and maintenance and life-cycle cost savings increased. All of this is achieved through a natural variation of the span and wing area with weight in order to maintain aerodynamic efficiency — an advantage that is possible with this configuration [29]. With respect to the commonality of applications, aircraft applications have also been demonstrated for a variety of military applications including freighter, stand-off bomber, troop transport, and tanker; details of military BWBs can be found in [30].

In addition to these possibilities for commonality, the BWB's previously-noted, naturally area-ruled shape could also reduce manufacturing costs associated with conventional aircraft, which must be manufactured with a varying cross-section, 'coke-bottle' fuselage in order to achieve area-ruling [60]. This highlights the potential for the BWB to perform at higher speeds at lower costs. Further cost savings are implied since the interior configuration of a BWB is no longer a challenge. In contrast, a conventional aircraft with a varying cross-section will also have varying seats abreast along the area-ruled portion of the fuselage [30]. In the case of the SAI design, the increased aerodynamic and structural efficiency are features which could help offset potentially higher operating costs of a silent engine design [8].

Safety

The rear location of engines on the BWB places shrapnel from a failed engine behind the pressure vessel, most flight controls, systems and fuel tanks. The pressure vessel, due to its unique structural requirements and the necessity to handle both wing bending and pressure loads, must be robust and will likely have substantial crashworthiness [31, 29]. In addition, in certain configurations, the passenger compartment and fuel are separated by broad cargo bays [31].

Stability And Flight Control

Liebeck noted that a complicated high-lift system is not required for the Boeing design due to the low effective wing loading of the configuration. Redundance and reconfigurability of the trailing edge flight controls for this design are also discussed [31]. Furthermore, a reduction in the secondary power required by the control system is also demonstrated [30].

Other

Other potential benefits include increased loading and off-loading times due to the shorter fuselage length on a medium-sized (200-passenger) BWB [48], as well as a shorter take-off field length without the need for complicated high-lift devices [47].

1.2.2 Disadvantages of the Blended-Wing-Body

Despite the promise of the BWB, certain challenges exist.

Aerodynamics

For instance, atypical transonic airfoils of high thickness to chord ratio — up to about 17% in the Boeing designs [29] — are required inboard to accommodate passengers, cargo and landing gear. Furthermore, adding to the difficulty of the design of such

airfoils, this thickness to chord ratio must be maintained along a considerable portion of the chordlength [52, 29]. This poses problems for maintaining low drag [76]. In addition, due to deck angle limitations, the centerbody airfoils must be designed to generate the necessary lift at angles of attack which are consistent with deck angle requirements [52, 59, 29].

Supersonic flow on the lower surface of the BWB is another challenge, which is not typical on the conventional configuration [52]. Smooth transition from the thicker centerbody airfoils to the thinner outer wing airfoils can also be cause for difficulty, particularly for medium-sized 200-passenger BWBs since the transition could be more abrupt for such smaller aircraft [48]. Additionally, the benefit of the reduced wetted area may not hold in all cases; for instance, Pambagjo *et al.* pointed out that achieving the wetted area reduction could be more challenging in the case of a medium-sized BWB aircraft, which was, in fact, found to have a higher wetted area when compared to conventional aircraft [48]. Finally, while BLI techonologies and embedded engines sound promising, challenges with the integration of the engine and airframe and incorporation of these technologies include the design of low-loss inlet ducts, the control of the inlet flow distortion, and the turbomachinery integration [8]. In the aerodynamic design of the aircraft, manufacturing constraints must also be factored in: complex, three-dimensional shapes which might be expensive and difficult to manufacture must be avoided with smooth, simply curved surfaces being favoured [59, 29].

Propulsion

Additional difficulties of aft-mounted engines and propulsion and airframe integration exist, since engine integration affects several disciplines more directly than is the case for conventional aircraft [76, 31]. Indeed, interaction between the wing, control surfaces, and engines increase the complexity of the design of this region [59]. Liebeck *et al.* explore solutions for this issue in [31].

Structures

A key challenge is posed by the BWB's non-cylindrical pressure vessel, which must be light-weight yet capable of handling both the wing bending loads as well as the cabin pressure loads. As shown in [41], a box-type BWB fuselage could have stress about an order of magnitude higher than the stress in a cylindrical pressurized fuselage. The increased stresses in such a pressure vessel naturally lead to increased structural weight [31, 74]. Mukhopadhyay *et al.* [42, 41] and Velicki *et al.* [73] discuss detailed concepts considered specifically for the BWB configuration. Mukhopadhyay *et al.* study different concepts in order to determine the optimal fuselage configuration for the BWB including multibubble fuselage models: two, three, four, and five bubble models [42, 41]. Through this study an overall weight reduction of 20-30% compared to using all flat surfaces could be achieved through the proper integration of partially cylindrical surfaces in pressurized fuselage design. In [41], a Y-braced 480-passenger aircraft fuselage which develops into a modified fuselage in which the Y-brace is replaced by a vaulted shell is also discussed. Velicki *et al.* present the technology likely incorporated in this Y-braced configuration: Pultruded Rod Stitched Efficient Unitized Structure (PRSEUS) — a technology specifically designed, tailored and optimized for the BWB airframe [73]. Features of this technology include continuous load paths in two directions, accommodating the unique spanwise and streamwise load paths of the BWB fuselage, thin skins which operate in the post-buckled design regime, and stitched interfaces to arrest damage propagation. The pressurized shell elements (skin panels and frames) have also been found to be 28% lighter for the PRSEUS concept than comparable sandwich panel designs.

Stability And Flight Control

The integrated nature of the BWB, along with the elimination of the tail, means that interactions between inertial forces, aerodynamic loads, elastic deformations and the flight control system responses may have great impact on the performance and stability

of the aircraft [29, 74, 66]. Several issues arise: the aircraft must be balanced while ensuring control deflections do not adversely affect the spanload and drag [76]. For larger BWBs, such as those considered by NASA and Boeing, control surface hinge moments are substantial [59]. Thus, if the aircraft is unstable and dependent on active flight controls, secondary power requirements could be prohibitive [76, 59, 29].

Marketing And Manufacturing

While the BWB might present a more spacious environment, there are some potentially negative aspects that make marketing of this configuration a challenge. First, with a window only in each main cabin door and no other windows on the cabin walls, passengers might be uncomfortable in a BWB. A proposed solution is to use flat display screens connected to an array of digital video cameras to make every seat a window seat [29]. Secondly, given the lateral offset from the center of gravity, the ride quality could deteriorate in the outer portions of the BWB. Boeing has performed a series of tests in which piloted flight simulator tests of the BWB-450 and B747-400 using the same pilots and flight profile were carried out for different cases. The comparisons found the ride quality only decreased slightly — about 4% using the NASA Jacobsen ride quality model to determine passenger satisfaction with the ride — for both the best and worst seats on both aircraft [30, 29]. Finally, a minor marketing issue with respect to commonality in a family of BWB aircraft is extra weight on smaller members of the family compared to stand-alone BWB models [30]; however, a relaxation in the requirement that the members have common part numbers permits a skin gauge change, reducing the weight penalty substantially [29].

Certification

Finally, certification of the BWB might be hindered due to concerns of efficient emergency egress [29]. This could be more problematic for larger BWBs where the distance from the

exits increases [1] and lack of clear views of the different exits on larger BWBs will create challenges for cabin crew redirecting passengers [10]. However, both Bolsunovsky *et al.* and Liebeck argue that procedures compliant with FAR-25 can be implemented [1, 29]. Liebeck argues that passengers have a direct view of one or more exits, without requiring a 90 degree turn to reach the door from the aisle. This is accommodated by the fact that the Boeing design has a main cabin door directly in front of each aisle and an exit through the aft pressure bulkhead at the rear of each aisle. In addition, four spanwise aisles intersect with these longitudinal aisles [29]. Both computer simulations and full-scale evacuation trials carried out by Galea *et al.* for a 1000+ passenger BWB aircraft showed that improved visual access and awareness of the aircraft layout are key to efficient egress in emergency situations. Fire simulations found 12 fatalities deemed inevitable but independent of the cabin architecture [10].

Other

Other issues include landing approach speed and attitude and buffet and stall characteristics [59, 29]. In addition, other studies of BWB have shown engines arranged on pylons under the wing [1], which would eliminate a lot of the benefits outlined with respect to noise and drag reduction previously discussed.

1.2.3 Previous Studies and Key Findings

Flying wing configurations have been of interest for many decades now. In the 1940s, the world's first jet-powered flying wing, the Horten Ho 229, was one of the aircraft designed by the Horten brothers for use by the Nazi party during World War II. Though the prototype was captured by Allied forces, it is thought that the stealth and speed advantage of this advanced aircraft design over the conventional aircraft of the time could have significantly changed the outcome of the war [43].

Interest in blended-wing-bodies and flying wing configurations has continued to grow

over the years. The BWB configuration is essentially a flying wing which must carry a payload, produce lift with minimum drag penalty and provide the necessary stability and control [48]. This makes for a highly integrated aircraft configuration which ultimately requires advanced research and multi-disciplinary technology and design methods [25]. Both challenges and opportunities are present with this configuration; however, with sufficient research and study, despite the challenges, these opportunities can provide significant advantages over existing aircraft which might not otherwise be attainable. Several research projects, some of which have already been mentioned, attempt to explore these possibilities and study the challenges in greater depth. These are described next.

NASA Projects (USA)

In the hopes of setting in motion 'a renaissance for the long-haul transport', a study of the BWB configuration [31] began with a focus on aerodynamics [52] and evolved to more detailed, multi-disciplinary considerations over the years [30, 29, 31, 59]. A preliminary comparison consisting of a streamlined disk versus a tube and progressing with the addition of key aircraft components showed a potential total wetted area reduction of about 33%, which translates into an increased lift-to-drag ratio and motivated further study of this concept [29].

The initial development and feasibility study involved the set-up of a NASA-industry-university team in 1994. This team conducted a 3-year study demonstrating the commercial and technical feasibility of the BWB concept. Members of the team included McDonnell Douglas as program manager, NASA Langley Research Center, NASA John H. Glenn Research Center at Lewis Field, Stanford University, University of Southern California, University of Florida, and Clark-Atlanta University. Several design constraints were considered in the design of an 800-passenger BWB with a 7000 nautical mile range: volume, cruise deck angle, landing approach speed and altitude, buffet and stall, trim, power for control surface actuation, and manufacturing. For aerodynamics, Navier-Stokes

computational fluid dynamics (CFD) methodology in both inverse design and direct solution modes were employed to define the final BWB geometry. In addition, transonic and low-speed wind tunnel tests were carried out at NASA Langley Research Center's National Transonic Facility, resulting in excellent agreement between experimental and computational results. For structures, two concepts were studied: a thin, arched pressure vessel above and below each cabin which takes the load in tension and is independent of the wing skin, and a thick sandwich structure for both the upper and lower wing surfaces which handles both cabin pressure loads and wing bending loads. For the former, a potential pressure leak is a point of concern. In this case, Mukhopadhyay *et al.* state that the outer ribbed shell provides adequate redundancy and is found to be strong enough to withstand operational cabin pressure [42]. However, Liebeck argues that once sized to carry this outer pressure load, the outer wing skin is sufficient, eliminating the need for an inner pressure vessel; consequently, the thick sandwich concept was chosen for the centerbody structure [29]. More recently, Velicki *et al.* have proposed the PRSEUS concept described earlier [73]. Boundary layer ingestion studies were carried out at both University of Southern California and Stanford University, with the latter performing multidisciplinary optimization studies of the BWB engine inlet concept based on the wind-tunnel simulations carried out by the former [29, 31]. Using a 6% scale flight control testbed built at Stanford University, low-speed flight mechanics were explored and excellent handling qualities within the normal flight envelope were demonstrated. Overall, with significant weight reduction and one less 60,000lb class engine, the fuel burn per seat mile was found to be 27% lower compared to a conventional aircraft.

This study subsequently developed into the study of the BWB-450 — a 450-passenger aircraft deemed more in line with market forecasts and a reasonable comparison to existing aircraft such as the A380, B747, and A340. Using Boeing's proprietary code, WingMOD, MDO was carried out with a vortex-lattice code and monocoque beam analysis coupled to give static aeroelastic loads. A new class of transonic airfoils was designed.

These airfoils not only smoothened and flattened the goemetry for simplified manufacture, but also accommodated the cross-sectional area requirements for payload. Structurally, an 18% reduction in the BWB-450's MTOW relative to an A380-700 was achieved. The fuel burn per seat was 32% lower than the A380-700. Aspects of stability, propulsion, environment and performance are discussed in more detail by Liebeck [29], as are unique opportunities and challenges — as discussed in the previous section: manufacturing part count, family and growth opportunities, speed opportunities, passenger acceptance, ride quality and emergency egress [29].

In addition to these studies, as part of the NASA Revolutionary Aerospace Systems Concepts Program, the Quiet Green Transport (QGT) study [17], aimed at developing and evaluating commercial transport aircraft concepts that significantly reduce or eliminate aircraft noise and emissions, as well as identifying technology advances essential to the feasibility of the concepts, considered the BWB configuration with distributed hydrogen fuel cell propulsion. Assuming the availability of certain advanced technologies, project benefits relative to today's conventional aircraft include complete elimination of all aircraft emissions except H_2O, the possibility of eliminating the formation of persistent contrails, 10% reduction in the area exposed to noise levels of 55dBA and greater during takeoff and landing operations, and 8 to 22dB EPNL reduction in noise at FAA noise certification points. Despite these advantages, several areas will need to advance significantly to realize the full potential of the concept. For instance, even with 25-30 year projected improvements, conventional aircraft engines are still lighter than the fuel cell based system which would rely on liquid hydrogen [17]. While the concept might be difficult to achieve at this point, the versatility of the BWB is clearly demonstrated.

Multidisciplinary Optimisation Of A Blended Wing Body (MOB) Project (Europe)

The collaborative **M**ultidisciplinary **O**ptimisation of a **B**lended Wing Body (MOB) [40] project between universities, research institutes and companies across the UK, Germany, Netherlands, and Sweden has the primary goal of developing a variety of discipline-based (aerodynamics, structural, aero-elastic and flight mechanics) commercial or proprietary programs and tools to enable a range of studies from preliminary, rapid assessments of initial configurations to high-quality, expensive computational simulations and assessments by distributed design teams. Essentially, this distributed yet integrated system, the Computational Design Engine (CDE), is a multi-level, multi-site, multidisciplinary design tool. A secondary goal of the project is to apply the CDE to the BWB aircraft.

At Sheffield University, Qin *et al.*'s contributions to the MOB project include various aerodynamics studies of the BWB [53]. Both high-fidelity RANS evaluation with a Baldwin-Lomax algebraic turbulence model and Euler equations are used in the design process, with key considerations being wave drag, spanwise load distribution, aerofoil section design and 3D shaping for performance improvement. First, an inverse design of the spanwise loading employed a panel method with three target loadings: elliptical — reduces induced drag, triangular — reduces wave drag, and an average of the two — a compromise, with the goal of alleviating high wave drag by shifting the load inboard. Significant wave drag reduction on the outer wing was achieved for the new twist distributions with the averaged distribution having the minimum total drag and thus, the highest aerodynamic efficiency. The loading on all three designs is moved inwards towards the centerbody relative to the baseline loading, with the highest centerbody loading for the triangular distribution and lowest for the elliptical. Structural and stability advantages to the averaged distribution are highlighted in [53, 54].

Subsequently, starting from the twist inverse design results, airfoils were mapped from 3D to 2D, optimized, and mapped back to 3D. The resulting geometry had a 20%

increase in lift-to-drag ratio compared to the baseline; however, the high sweep and 3-dimensionality of the BWB shape implies 2D optimization cannot fully capture the potential of shape optimization, leading to the final portion of the study: 3D Euler aero surface optimization, incorporating a twist and camber optimization with pitching moment constraint and 3D surface optimization with trim constraint. The twist inverse design previously obtained was used as the starting geometry. Minimizing pressure drag was deemed crucial since it dominates the total drag due to the lower surface to volume ratio. In addition, the optimal spanwise lift distribution for best aerodynamic performance should be a fine balance of induced drag due to lift and wave drag due to shock wave formation at transonic speeds, such as the average elliptical/triangular distribution studied. As such, the elliptic distribution should no longer be the target for minimum drag design, unless wave drag can be eliminated by the design optimization, in which case an elliptic distribution may still be favourable for aerodynamics [63].

Further studies done by Qin *et al.* involve BWB configurations with forward swept wings [63], varying the outer wing sweep angles, defined as the leading edge sweep of the wing, from -40 degrees (forward sweep) to 55 degrees (backwards sweep), keeping planform fixed and using a pitching moment constraint. The lift-to-drag ratio for forward swept wings was low and relatively constant as forward sweep angles were increased. In this case, the wing sweep cancels with the sweep of the body, creating intense shocks at the junction between the two. Increased contributions to the wave drag result in the trend observed. In contrast, for 0 to 55 degrees, the lift-to-drag ratio increased substantially and peaked at 45 degrees. Other interesting studies include the control of shock waves on the BWB via 3D shock control bumps [78].

Tohoku University (Japan)

Pambagjo *et al.*'s research [47, 48] aimed to design a regional BWB aircraft for about 224 passengers, a cruise Mach number of 0.8 and a range of 2000 nautical miles. Using a

Navier-Stokes flow solver with a fully turbulent boundary layer (Baldwin-Lomax turbulence model), an inverse design and target pressure specification technique were carried out. The first step of this process was to design the target pressure distribution based on the required aerodynamic performance. For the initial design [48], the specified target pressure distribution was obtained with discrepancies at the leading and trailing edges. The outboard wing was inversely designed with the goal of elliptical loading, while ensuring sufficient fuel volume. The inboard section was designed as thin as possible without sacrificing too much of the internal space and comfort. For the follow-up design [47], shocks were eliminated on the upper and lower surfaces and agreement with the target elliptical span loading was improved; however, the pitching moment was slightly higher for this configuration than for the final configuration initally presented [48].

TsAGI (Russia)

This work — done in conjunction with Airbus and Boeing — placed emphasis on the rationale behind the main design of flying wing configurations and developing and analyzing alternative configurations, while taking the aerodynamic and structural concepts into consideration. The analysis process consisted of three stages: first, development of a baseline configuration to define the project requirements; second, development of three candidate concepts: an integrated wing body (IWB), a lifting-body configuration, and a pure flying wing — all designed for the same requirements for a fair comparison; and third, detailed computational and experimental studies for the most promising layout. With a design mission for 750 passengers, 13,700 km range and cruise Mach number of 0.85, comparisons of the alternatives to the conventional configuration on the basis of aerodynamics, weight, fuel efficiency, etc., led to the selection of the IWB configuration. This configuration maintains the high L/D advantage of a flying wing at about 24.5 for a Mach number of 0.85, maintains structural efficiency, and meets all the main requirements of FAR-25 [1].

MIT/Cambridge Silent Aircraft Initiative (SAI) (USA/UK)

Given its aerodynamic advantages, noise reduction, and characteristic cost savings, the BWB configuration was an ideal option for SAI's goal of designing an aircraft which is inaudible outside the airport boundary in a typical urban area [69, 8, 9]. Diedrich *et al.* combined WingMOD [75], an established MDO tool also utilized by Boeing, which incorporates aerodynamics, loads, performance, weights, balance, stability and control considerations with first principles and empirically-based design and acoustic prediction methods, to explore an unconventional BWB aircraft configuration to achieve the stated goal, while also ensuring competitive performance with next-generation aircraft such as the B787 [8]. Based on a design mission of 215 passengers, a range of 5000 nautical miles, a cruise Mach number of 0.80, and technology levels consistent with 2030 entry to service, an optimized aircraft which achieves significant noise reduction compared to similar, existing commercial aircraft was obtained; however the goal of being inaudible outside of the airport perimeter was not achieved and further technology developments were deemed necessary. The optimized aircraft fuel burn was competitive with B787-type aircraft, as desired.

Other interesting outcomes of the project include research into the use of leading-edge carving which enables the entire planform to generate lift (an 'all-lifting' design) and produces a final aircraft which is both balanced and statically stable — without the use of a reflexed airfoil, for instance [69, 62]. Additional research into landing gear studies [56], Boundary Layer Ingestion studies [51], continuous descent [58] and surface roughness [32] are examples of the types of projects that have and are developing out of this project.

Israel Aircraft Industries (Israel)

With the goal of developing an aircraft configuration with minimum drag at cruise conditions while satisfying defined constraints, Peigin and Epstein [50] employed the NES

multiblock code, a Navier-Stokes flow solver, in single and multipoint optimizations with a genetic algorithm. The baseline geometry was the same used by Qin *et al.* [53]. The main design point in the multipoint optimization required a lift coefficient of 0.41 and Mach number of 0.85, also consistent with Qin *et al.* The off-design points considered a high Mach number case for drag divergence behaviour: Mach 0.87; and a take-off condition: Mach 0.2. The objective function of the multipoint optimization problem is a weighted combination of the drag coefficients, C_D^{wtd}, at all design points, with weight factors based on the relative importance of the design points as determined from experience. For the single-point optimization, the shock was eliminated and the initial drag count of 247 dropped to 194.5 counts. A second single-point optimization with a pitching moment constraint resulted in a 1.9 drag count increase between the two single-point optimization results. From the multi-point (three-point) optimization, the drag divergence Mach number is increased from 0.855 (one and two-point optimizations) to 0.87. Furthermore, the C_L^{max} is also increased significantly relative to the baseline shape via the inclusion of take-off conditions. Finally, a 20 and 29% reduction in drag for the main and higher Mach number secondary design points was also achieved, along with the target maximum lift coefficient at take-off conditions [50].

Universidad Politécnica de Madrid (Spain)

Martínez-Val *et al.* [34] showed a medium-sized C-wing flying wing for 300 passengers was operationally efficient and preferable to conventional airplanes of similar capacity. The horizontal stabilizers incorporated on the C-wing portion of the body are considered useful for stability and control improvements. Compared to the A330-200 and B777-200, the take-off and landing field lengths are shortened for the C-wing. Fuel burn is found to be 19.8g/passenger-km — less than the 21.5 and 23.5g/passenger-km for the A330 and B777, respectively. Extending this work, a comparison of the C-wing with a U-wing flying wing aircraft (a flying wing with vertical winglets) was carried out with a study of

how relevant, emerging technologies such as laminar flow control (LFC), vectored thrust, and active stability can provide additional improvements [34]. The U-wing configuration along with the emerging technologies resulted in a fuel efficiency of 14.6g/passenger-km — the lowest of all the options considered. Overall, both the C-wing and U-wing configuration present significant advantages over the conventional layouts; however, it is important to note that while the U-wing configuration is lighter, for this design, it requires vectored-thrust which is currently unavailable for civil aviation [34].

Airbus Projects (Europe)

Airbus is involved in various projects with ONERA and DLR as major collaborators, in addition to other companies and institutions. The **V**ery **E**fficient **L**arge **A**ircraft (VELA) project has Airbus as the leading company with 17 European partners from industry and research working together to extend their knowledge of BWB configurations [67]. AVECA, a national project carried out in close collaboration between Airbus and ONERA, focuses on lower capacity flying wing aircraft since this topic has not been as extensively evaluated as the larger counterparts [38]. Finally, the **N**ew **A**ircraft **C**oncepts **Re**search (NACRE) project is also led by Airbus with 36 partners [39, 38].

As part of VELA, each configuration studied in [67] was defined by two leading edge sweep angles on the inboard and outboard wing sections and a corresponding cabin geometry. Constraints included volume, deck cabin angle, and stability considerations. A DLR finite volume flow solver, FLOWer, which solves the 3D compressible Euler equations in integral form, was employed in this two part process consisting of 2D multipoint airfoil design optimization and a 3D twist and chord-length optimization. The 3D optimization employed GenOpt-software as the optimizer - specifically, the Nelder-Mead Simplex algorithm. Eight design variables, such as the change of twist and chord length with constant thickness to chord for the three outer wing sections, were used. Additional details can be found in [67]. The flow analysis was performed in Euler mode with

stripwise boundary layer analysis, using the integral method for friction drag estimation. Sixteen percent drag reduction with constant lift was achieved. The shock wave on the outer wing was modified from a strong single shock close to the trailing edge to a weaker double shock system; consequently, the drag reduction was dominated by wave drag reduction (63%). This wave drag reduction was achieved by increasing chord lengths in the outer wing and adjusting twist angles [67]; however, since wave drag was still present, the optimum lift distribution was not of elliptical form, which might be expected if total minimum drag is achieved [39]. Additional research includes the determination of static and dynamic derivatives for stability and handling characteristics, along with high-speed testing, to create an experimental database for aerodynamic performance assessment and **Se**mi-**Bu**ried engines (SEBU), through which engine installation effects are studied [39].

The AVECA project [38] studied lower capacity BWB configurations, aiming to design viable flying wing geometries considering aerodynamic cruise performance, longitudinal trimming constraints and geometric constraints such as cabin and landing gear volumes. Specific details of the design mission were excluded. Navier-Stokes, multiblock, structured flow solves for Mach 0.85, Re/c of 172.2 million per meter (Note: the units of Re/c are not specified in the paper and are inferred from geometry images) were carried out using the ONERA *elsA* code. Some of the goals included increasing the lift-to-drag ratio at the design point and avoiding strong shocks on both sides of the wing while meeting the various geometric constraints. A manual, iterative strategy with a total of 60 configurations was used to design the inboard section and ultimately suppress the shock. For the outboard section, optimization driven by the gradient algorithm, CONMIN, was used to define the twist distribution of the configuration. The total drag, considering constraints on lift and on the location of the center of pressure, made up the objective function. Two design points were considered: Mach 0.85, Re/c of 172.2 million per meter and Mach 0.87, Re/c of 176.3 million per meter. For the first point, a 9.5% and 39.1% decrease in viscous and wave drag was achieved, respectively; while for the second point,

these reductions were 18.9% and 37%, respectively [38].

Additional research under the NACRE project includes projects such as winglet design for large capacity flying wing configurations [38]. The winglet, equipped with control surfaces, is expected to provide substantial drag reduction and additional lateral stability. This concept with plain flap control surfaces is studied on a VELA2 configuration to demonstrate the efficiency of a winglet and to model its effects on control derivatives.

1.3 Problem Definition and Objective

The goal of this thesis is to bring together two key concepts — high-fidelity simulation and optimization tools and the blended-wing-body aircraft configuration — to see how optimization might be used to explore the design space and discover new and unconventional designs or aspects on the BWB shape. In particular, in this thesis, the following single-point, Euler-based optimizations are performed and discussed:

- Transonic optimizations with fixed airfoil sections
- Transonic optimizations with variable airfoil sections.

For these optimizations, the objective function — the sum of induced and wave drag — is minimized. The control points of the B-spline geometry parameterization used to represent the aerodynamic surface are used as the design variables. In addition to a lift constraint for a specific design mission, geometric constraints which, for instance, ensure that the main body section of the BWB provides sufficient volume for passengers and cargo are also included. Other constraints are also enforced to limit the freedom and aid the convergence of the optimization.

While the BWB concept is highly integrated in nature [52], the focus here is on aerodynamics only. A brief discussion of potential for and interest in aerostructural considerations is provided in Appendix A.

Multi-point optimizations which take into consideration multiple operating points, resulting in a design which is a compromise between various design requirements, are also of future interest. Details of the implementation and verification of multi-point optimization are provided in Appendix B.

Chapter 2

Baseline Geometry Definition

For a given design mission, minimum internal space requirements can be defined. An external, aerodynamic BWB shell is then created to envelop this internal volume. During the process of the creation of this outer shell, an appropriate lift coefficient target value for the optimization process can also be defined.

For these key aspects, a simple tool was developed to determine the minimum internal space requirements. In order to define the outer, baseline geometry of the BWB used in the optimizations, a B-spline based geometry parameterization is employed. Finally, a rough weight estimation process and the methodology used to obtain the target lift coefficient are also described.

Note that specific details of the design mission are excluded in order to keep the following description as general as possible.

2.1 Internal Volume Constraints

Sufficient space for crew, passengers, luggage, lavatories, and galleys is determined using a sizing tool developed with reference to [2] and [70]. For user-specified parameters, such as number of passengers, seat pitch, and height of the cabin, a polyhedron representing the minimum external bounds of the interior layout is generated. Based on the results,

minimum chord length constraint values and spanwise positions of these constraints can then be determined for the optimization process, along with target thickness and volume constraints.

Given the importance of the pressure vessel for the BWB configuration, it is important that there be sufficient space included as part of this polyhedron for this structure. As discussed in Section 1.2, two primary options considered by NASA and Boeing for the pressure vessel include:

- A separate outer skin with inner cylindrical shells for internal pressure (i.e. multi-bubbles)
- An integrated skin and shell

While NASA studies suggest the multi-bubble idea is optimal [42], Liebeck argues that the outer skin would have to be designed to handle internal pressures in case of a leak, making for an unnecessary redundancy, and thus leaving the second option as the more logical of the two. Bradley [2] deems a height of 8.25ft sufficient for the integrated skin and shell, passenger standing height, and furnishings.

2.2 Geometry Parameterization

B-spline-based surface patches — specifically, employing cubic B-splines — are used to parameterize the smooth aerodynamic geometries studied in this project. The control points of these cubic B-splines can then be used as design variables, enabling modification of the aerodynamic surface [20].

In principle, it is possible to consider almost arbitrary geometries within the feasible design space defined by the constraints. In practice, however, it is initially preferable to consider various baseline shapes with more limited flexibility. Using a B-spline-based geometry parameterization, various baseline BWB geometries can be generated. For this purpose, an existing parameterization was modified to include two more sections with

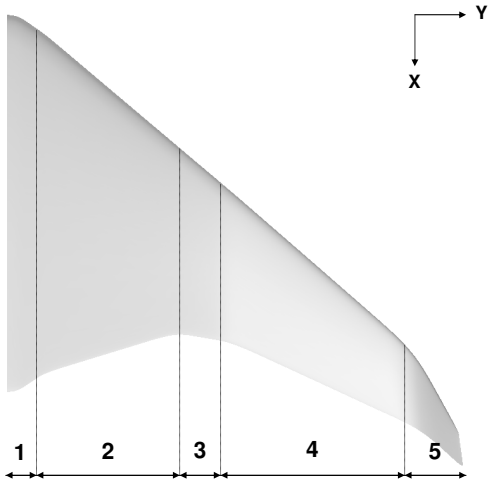

Figure 2.1: Blended-wing-body geometry representation.

increased capabilities such as the inclusion of twist, dihedral and sweep, along with the option to approximate different airfoils at each defined section of the BWB geometry.

Various BWB geometries can be generated with this B-spline-based geometry parameterization. As part of the parameterization, the aircraft is defined by five different sections, shown in Figure 2.1. For each of these sections, different airfoils may be specified and are fit with B-spline curves. The control point coordinates from this fitting are then used to define the x- and z-coordinates of the control points defining the B-spline surface patch for the baseline BWB, where the x-coordinates are in the chordwise direction. The y-coordinates, which are in the spanwise direction, are specified at equal intervals over the user-specified semi-span of the aircraft.

For sections 1 to 3 in Figure 2.1, the sweep, chord-lengths and span can be modified, defining the main body of the BWB. In addition to these parameters, twist and dihedral can also be added to sections 4 and 5, which make up the outer wing. Based on these parameters, the control point coordinate values in each direction are modified to generate the desired baseline shape.

Three sections are included for the main body of the BWB in order to increase flexibility in the geometry definition. This is particularly important with the long-term goal

of studying BWBs of various sizes and accommodating the internal volume requirements which might result. Two sections on the outer wing were deemed sufficient to define just a wing or a wing with a winglet. Keeping in mind the limitations of the parameters which can be applied to each section, it is important to note that these sections are by no means dedicated to either the main body or the outer wing. Rather this is just the definition employed for the baseline presented in this thesis. For instance, for a C-wing type BWB, the third section of the main body can be easily incorporated into the outer wing instead.

The parameters: sweep, span, chord-length, twist, and dihedral are considered from both a sizing and comfort perspective and an aerodynamics perspective. From a sizing perspective, enabling variation of the first three of these parameters allows for the accommodation of BWBs of various sizes. Keeping passenger comfort in mind, twist and dihedral are excluded on the first three sections. From an aerodynamics perspective, enabling variation of these parameters, along with the airfoils at each section enables a more thorough definition of the baseline geometry, using the method described below for example.

For the baseline geometries included and studied in this thesis, supercritical airfoils — specifically variations of SC20414 [72] — are generally employed given their favourable characteristics under transonic conditions; however, an option which might result in an improved baseline geometry would be to follow a procedure similar to that in [53]: optimize 2D airfoils, using a tool such as Optima2D [3, 44] for instance, and then project them back to the 3D shape of the BWB. As noted by Qin *et al.*, this neglects the 3D effects of the BWB shape, but will still result in an improved baseline geometry and a more interesting starting point for the optimizer.

Figure 2.2 shows some sample baseline shapes generated using this parameterization, which can be used as a basis for optimization. For the optimization process, the initial baseline geometry is divided into a main body section and an outer wing section with

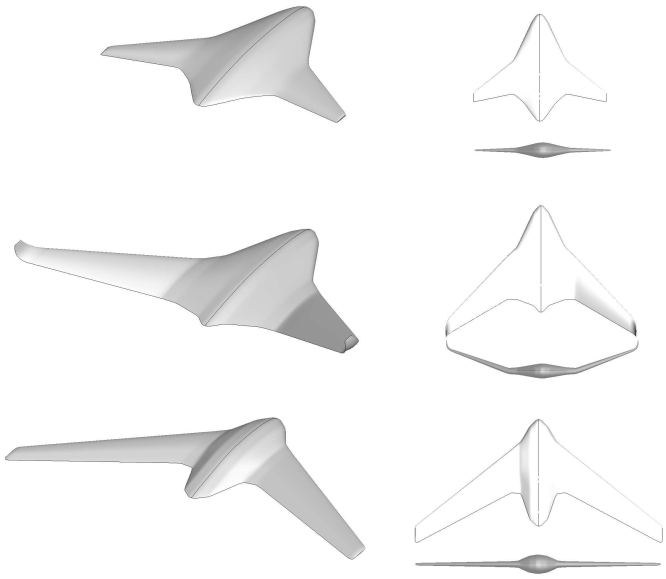

Figure 2.2: Examples of different baseline shapes which can be generated using the geometry parameterization.

fixed spans. Based on this definition, the shapes in Figure 2.2 differ from each other in that they lie in different design spaces. For instance, additional sections would be added for non-planar elements such as those in the second geometry in Figure 2.2. As such, it is beneficial to have a flexible geometry parameterization tool such as the one described here.

Ultimately, this reliance on the initial geometry will be eliminated. In this case, rather than using a fixed polyhedron as defined in the previous section, an internal geometry definition which evolves with the shape and serves as an internal volume constraint would be preferable, in order to ensure that the passenger seating, cargo, lavatory, galley, aisle space, etc. requirements are always satisfied by the shape.

2.3 Weight Estimation and Planform Area Sizing

Sizing the baseline geometry is not limited to ensuring that the outer BWB shell envelops the polyhedron representing minimum external bounds. Two additional factors are considered: weight estimation and planform area sizing, in order to ensure a rea-

sonable wing loading relative to an existing, comparable tube-and-wing aircraft. As a rough rule of thumb, based on data provided by Liebeck [29], a target wing loading of approximately 70% of that for a selected tube-and-wing aircraft was set. In addition, the target C_L value would need to fall within a reasonably expected range of values.

In order to obtain a rough weight estimate for the approximate target lift coefficient, a combination of equations were employed. The blended-wing-body was considered in three parts: the cabin, aft-body and wing, where the aft-body [2] refers to the non-pressurized region which presumably supports the engines and is located behind the rear bulkhead and passenger cabin. The weight values of the cabin and aft-body were calculated using equations from [2], while the weight of the wing was calculated based on an equation in [70]. For the former, the derived equations are based on regression analysis using data for larger BWB aircraft than that considered in this thesis; however, given the general lack of relevant BWB weight data or equations, this was deemed the best option for the time being. For the latter, the equation is a simplified approximation for civil airplanes with aluminum alloy cantilever wings. Furthermore, this equation is not applicable in the case of wing-mounted engines, making its application in this case appropriate.

The following summarizes the procedure followed to obtain the weight estimate: first,

$$TOGW = W_{\text{empty}} + W_{\text{fuel}} + W_{\text{payload}} \tag{2.1}$$

where $TOGW$ = take-off gross weight (lb), W_{empty} = empty weight, W_{fuel} = fuel weight, and W_{payload} = payload weight.

The aircraft empty weight can be further broken down:

$$W_{\text{empty}} = W_{\text{cabin}} + W_{\text{aft-body}} + W_{\text{wing}} + W_{\text{fixed}} \tag{2.2}$$

where W_{cabin} = weight of the cabin section of the BWB, $W_{\text{aft-body}}$ = weight of the aft-body, W_{wing} = weight of the outer wing, W_{fixed} = weight of various components such as

furnishings, etc.

Based on these breakdowns, the various values for the weights are calculated.

Payload The payload weight consists of constant passenger and crew weight values plus their luggage weight based on data in [70].

Fuel A fuel weight value is assumed based on existing values for the reference aircraft of choice. This is obviously not the best method since fuel weight depends on aerodynamic properties, weight and design range; however, this is a preliminary estimate. Though based on conventional aircraft, an alternative method might be to follow the preliminary steps outlined by Raymer in [57] for a simplified mission profile.

Fixed weight Aircraft component weight values for furnishings, electrical components, air conditioning, etc. are based on averaged values for existing tube-and-wing aircraft of comparable size [26, 61] to the aircraft under consideration, assuming that these values would be roughly consistent between the two types of configurations. As with the payload and fuel weight, these values are fixed.

Cabin The following equation [2] is used for the weight of the pressurized cabin portion of the BWB:

$$W_{\text{cabin}} = (5.698865)(0.316422)(TOGW)^{0.166552}(S_{\text{cabin}})^{1.061158} \tag{2.3}$$

where S_{cabin} is the cabin planform area (ft^2).

Aft-body For this portion, the following equation also from [2] was used.

$$W_{\text{aft}-\text{body}} = (1 + 0.05N_{\text{eng}})(0.53S_{\text{aft}}TOGW^{0.2})(\lambda_{\text{aft}} + 0.5) \tag{2.4}$$

where N_{eng} = number of engines on the centerbody, S_{aft} = planform area of the

aft centerbody (ft^2), and λ_{aft} = taper ratio. Note that this aft-body portion was excluded for the design mission presented in the next section.

Wing From [70], the following equation is used for the weight of the outer wing:

$$\frac{W_{wing}}{W_G} = k_w b_s^{0.75} \left[1 + \sqrt{\frac{b_{ref}}{b_s}}\right] n_{ult}^{0.55} \left[\frac{b_s/t_r}{W_G/S}\right]^{0.30} \tag{2.5}$$

where for transport category aircraft $k_w = 1.7\text{x}10^{-3}$ = factor of proportionality for the weight of a group of items, W_G (lb) = $MZFW = TOGW - W_{fuel}$ = gross weight, $b_s = b/\cos(\Lambda_{1/2})$ = structural span (where b = wing span (ft), $\Lambda_{1/2}$ = sweepback angle at 50% chord (rad)), b_{ref} = 6.25ft = reference span, n_{ult} = ultimate load factor, t_r = (absolute) maximum thickness of root chord (ft), and S = (projected) area of a surface (ft^2).

As can be noted from the equations above, the weight estimation is also dependent on the planform area. Once this is specified, along with the rest of the variables, the three weights — W_{cabin}, $W_{aft-body}$, and W_{wing} — are all dependent on TOGW, which can then be solved for. Given this relationship, the assumed rough rule of the thumb for wing loading, and the target C_L considerations, the planform area was manually modified and iteratively sized around the internal volume polyhedron.

2.4 Baseline Geometry

Following the procedure outlined above, the baseline external BWB shape is manually determined, taking the weight estimation and planform sizing into account. The relevant geometric and performance parameters are outlined in Table 2.1. Figure 2.4 shows different views of the baseline geometry, which, as previously mentioned, employs variations of the supercritical SC20414 airfoil [72].

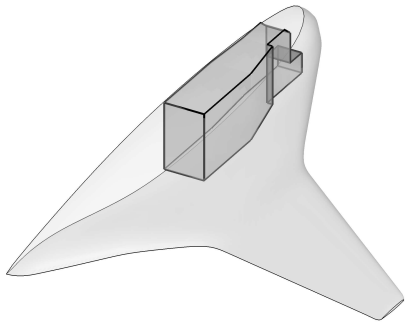

Figure 2.3: Half of the baseline BWB geometry with internal volume constraints.

Geometric Parameter	
Aspect Ratio	3.17
Performance Parameters	
C_L	0.357
Cruise Mach Number	0.85

Table 2.1: Key geometric and performance parameters for baseline BWB geometry.

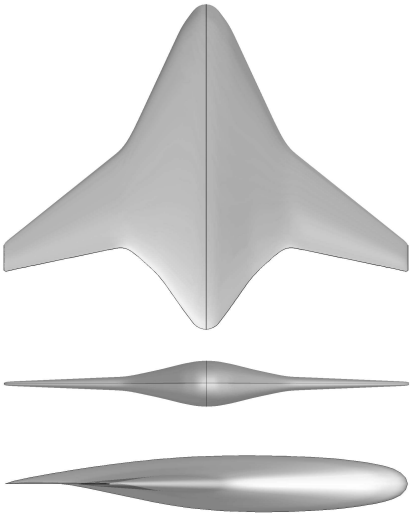

Figure 2.4: Baseline geometry planform, frontal and side views.

.

Chapter 3

Flow Analysis

The flow analysis in this thesis is performed using a parallel Newton-Krylov-Schur flow solver for the Euler equations governing inviscid, compressible flow on multiblock, structured meshes [18, 19].

3.1 Governing Equations

The three-dimensional Euler equations are given by

$$\partial_t \mathbf{Q} + \partial_{x_i} \mathbf{E}_i = \mathbf{0} \tag{3.1}$$

where

$$\mathbf{Q} = \begin{pmatrix} \rho \\ \rho u_1 \\ \rho u_2 \\ \rho u_3 \\ e \end{pmatrix}, \qquad E_i = \begin{pmatrix} \rho u_i \\ \rho u_1 u_i + p\delta_{1i} \\ \rho u_2 u_i + p\delta_{2i} \\ \rho u_3 u_i + p\delta_{3i} \\ (e+p)u_i \end{pmatrix},$$

$(x_1, x_2, x_3) = (x, y, z)$, δ_{ij} is the Kronecker delta, and the perfect gas law is assumed.

These equations are mapped to computational space to obtain the following:

$$\partial_t \hat{\mathbf{Q}} + \partial_{\xi_i} \hat{\mathbf{E}}_i = \mathbf{0} \tag{3.2}$$

$$\hat{Q} = \frac{1}{J} \begin{pmatrix} \rho \\ \rho u_1 \\ \rho u_2 \\ \rho u_3 \\ e \end{pmatrix}, \qquad \hat{E}_i = \frac{1}{J} \begin{pmatrix} \rho U_i \\ \rho u_1 U_i + p \partial_x \xi_i \\ \rho u_2 U_i + p \partial_y \xi_i \\ \rho u_3 U_i + p \partial_z \xi_i \\ (e+p) U_i \end{pmatrix},$$

where $(\xi_1, \xi_2, \xi_3) = (\xi, \eta, \zeta)$, J is the Jacobian of the mapping, and $U_i = u_j \partial_{x_j} \xi_i$ are the contravariant velocity components.

Using second-order accurate summation-by-parts (SBP) operators and scalar numerical dissipation, the Euler equations are discretized on each block. Simultaneous-approximation terms (SATs) are used to impose boundary conditions and couple block interfaces. Advantages to using SATs with SBPs include time-stability, minimum requirement of C^0 mesh continuity at block interfaces, accommodation of arbitrary block topologies, and low interblock communication overhead.

A parallel Newton-Krylov-Schur solution strategy is used to solve the discrete Euler equations. In particular, Newton's method is applied to the discrete Euler equations in two phases: an approximate-Newton phase which ensures a suitable initial iterate is found for the second phase, an inexact-Newton phase. In order to solve the systems that arise in both these phases, a Krylov solver is employed. Specifically, FGMRES — Flexible Generalized Minimum RESidual method — is employed along with the parallel additive-Schur preconditioner. For additional details behind the flow solver, the reader is referred to [18].

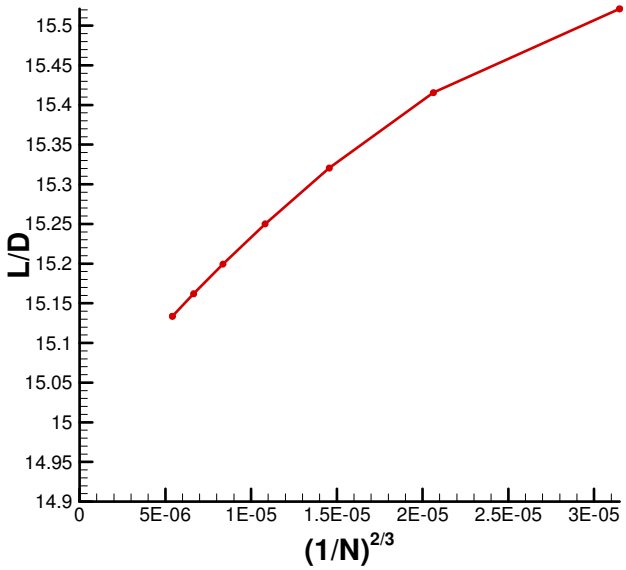

Figure 3.1: Grid convergence plot.

3.2 Grid Convergence Study

Given that the meshes employed in this thesis are relatively coarse, a grid convergence study was carried out to gain a better understanding of the relative amount of error in the results. Starting with a fine mesh of 79,396,992 nodes and 1,152 blocks, a family of meshes was generated by coarsening this fine mesh of the baseline geometry. Each mesh was run at a Mach number of 0.85 and angle of attack of 1 degree. Figure 3.1 shows the lift-to-drag ratio plotted against $(\frac{1}{N})^{\frac{2}{3}}$, where N is the number of nodes in the mesh. Based on this plot, the use of a coarse mesh appears to result in over-predictions of the ratio. This should be kept in mind for both the baseline and optimized geometries presented.

3.3 Baseline Geometry Analysis

The baseline geometry used for this flow analysis and the subsequent optimization studies is that shown in Figure 2.4. A clean geometry without control surfaces or propulsion components is studied. Furthermore, it is assumed that the aircraft is cruising at a Mach

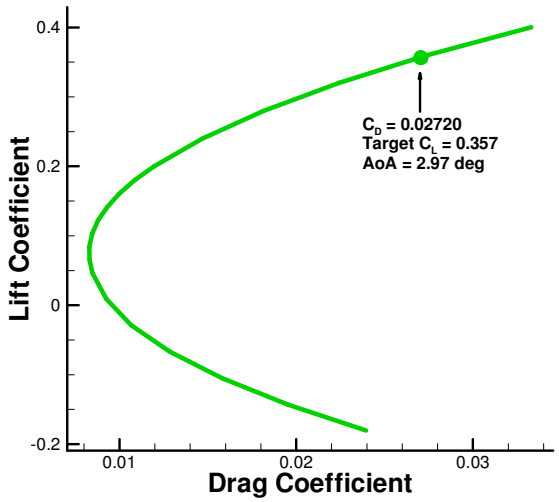

Figure 3.2: Drag polar for baseline BWB geometry.

number of 0.85. The present results were obtained using an 18-block mesh with 580,800 nodes and off-wall, leading edge, and trailing edge spacings of 0.005 root-chord units. Figure 3.2 shows the drag polar of the baseline geometry, which will be compared to that for the optimized geometry. The target C_L of the baseline geometry, 0.357, is obtained at an angle of attack of 2.97 degrees, resulting in a C_D of 0.02720. Given this C_L value and our aspect ratio, the drag value in the case of minimum induced drag and zero wave drag would be 0.01280, indicating potential for improvement on this baseline shape.

Figure 3.3 shows the pressure coefficient plots at the specified spanwise locations and indicates the presence of a strong shock on the top surface, including the main body surface. The airfoil sections for this baseline geometry are also shown. From Figure 3.4, with a maximum Mach number of almost 1.89, it is evident that this shock is quite strong. These results indicate wave drag is likely a major component of the total drag, indicating further potential for improvement.

From Figure 3.5, the presence of induced drag in addition to this wave drag is evident, given the discrepancy between the actual and optimal, elliptical spanwise load distributions.

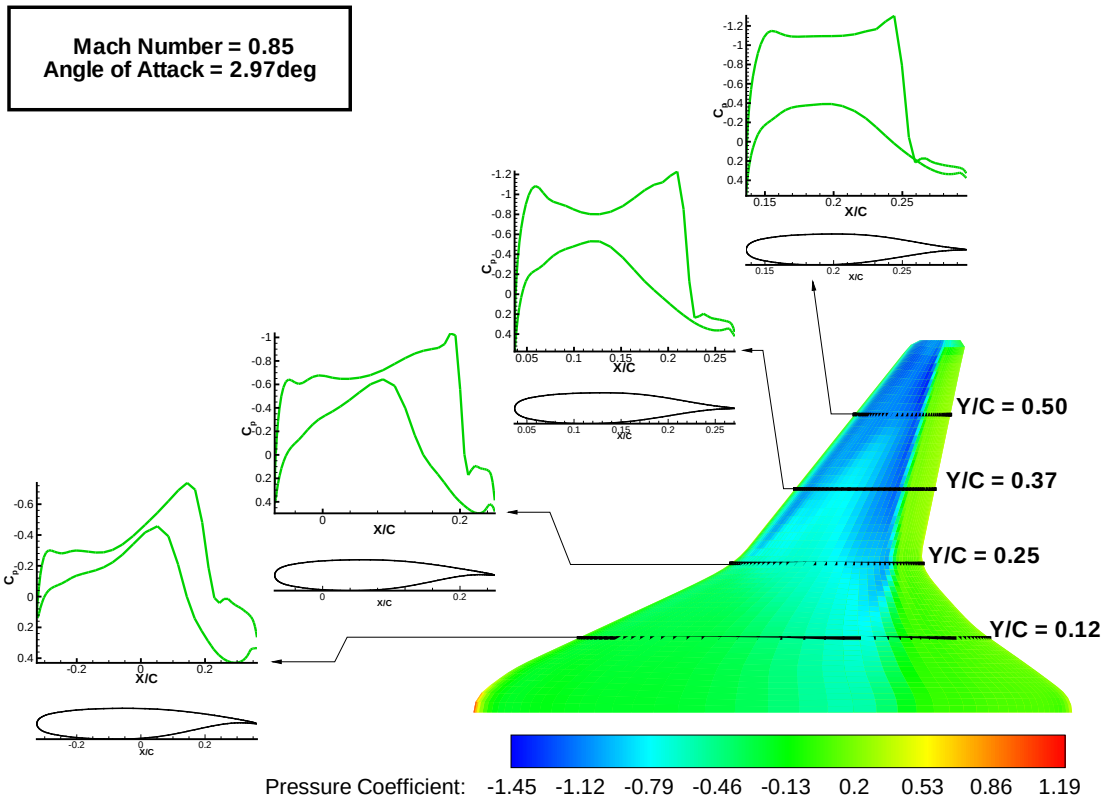

Figure 3.3: Pressure coefficient distribution over the top surface of the baseline BWB geometry and at indicated spanwise locations.

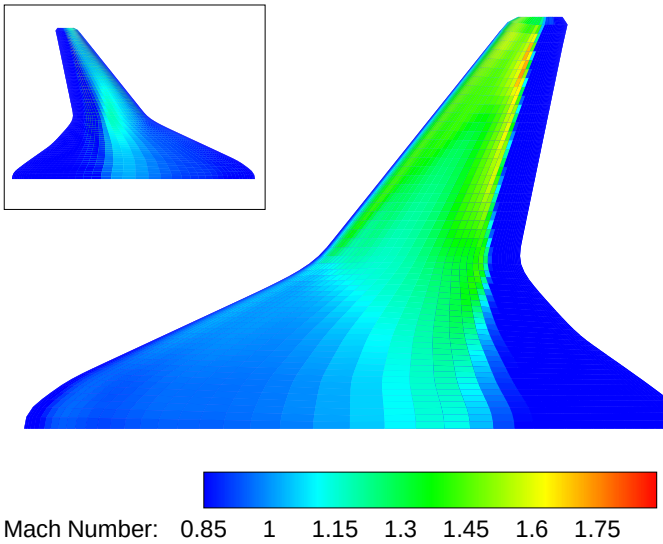

Figure 3.4: Mach number distribution over the top and bottom (inset) surfaces of the baseline BWB geometry.

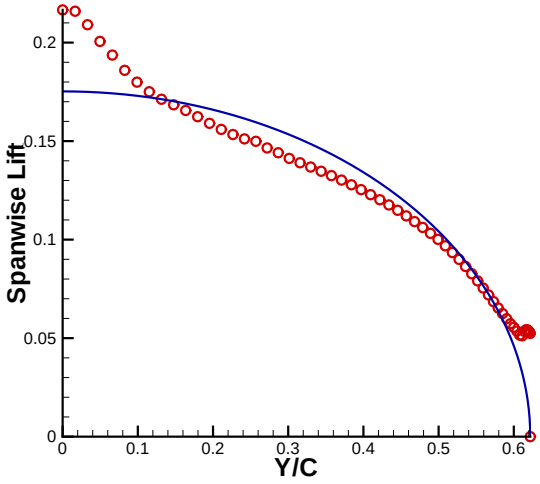

Figure 3.5: Baseline geometry spanwise load distribution.

Chapter 4

Optimization Tools

In order to carry out the optimization process, the following key components are necessary in addition to the flow solver described in the previous chapter. Details of these components can be found in [18].

4.1 Integrated Geometry Parameterization and Mesh Movement

For fast, robust, and flexible mesh movement for the design of unconventional aircraft such as the blended-wing-body, an integrated geometry parameterization and mesh movement algorithm is used [18, 20]. B-spline volume control points are used to parameterize the mesh. The geometry is parameterized as a B-spline surface, and the B-spline control points are used as design variables. For the movement of the B-spline volume control points, a linear-elasticity-based mesh movement is used. The mesh is then regenerated algebraically.

4.2 Adjoint-Based Gradient Evaluation

Consider the following generalized form of the optimization problem, based on notation in [18]:

$$\begin{aligned} \min \quad & \mathcal{J}(q, b^{(m)}, v) \\ \text{w.r.t} \quad & q, b^{(m)}, v \\ \text{s.t.} \quad & \mathcal{M}^{(i)}(b^{(i)}, b^{(i-1)}) = 0 \quad i \in \{1, 2, ..., m\} \\ & \mathcal{F}(q, b^{(m)}) = 0. \end{aligned}$$

That is, we wish to minimize $\mathcal{J}$, the objective function, which depends on q, the flow variables, $b^{(m)}$, the B-spline control points for the final mesh movement increment, denoted by m, of a series of increments, v, the design variables, which consist of the angle(s) of attack and geometric design variables. These geometric design variables are effectively a subset of the B-spline control points, $b^{(m)}$, including just those control points on the surface of the aerodynamic geometry being optimized. The optimization is subject to the constraints that $\mathcal{M}^{(i)}$, the grid movement residual vectors for the ith mesh movement increment and $\mathcal{F}$, the residual for the flow solver, are reduced to user-specified tolerances. For the optimization, the value of the objective function gradient is required. In order to obtain this gradient, an adjoint approach [21, 71] is employed and briefly described here.

For this optimization problem, the Lagrangian function, $\mathcal{L}$ is defined as follows:

$$\mathcal{L} = \mathcal{J} + \sum_{i=1}^{m} \lambda^{(i)T} \mathcal{M}^{(i)} + \psi^T \mathcal{F}, \tag{4.1}$$

where $\lambda^{(i)}$ and ψ, the Lagrange multipliers, are the mesh and flow adjoint variables, respectively, and each i is a step in the mesh-movement process. Additional details regarding the flow adjoint equation and mesh adjoint equations are available in [18].

Setting the partial derivatives of the Lagrangian with respect to the variables to zero, the following first-order optimality conditions, also known as the Karush-Kuhn-Tucker (KKT) conditions are obtained:

$$\frac{\partial \mathcal{L}}{\partial \lambda^{(i)}} = 0 = \mathcal{M}^{(i)}, \quad i \in \{1, 2, ..., m\} \tag{4.2}$$

$$\frac{\partial \mathcal{L}}{\partial \psi} = 0 = \mathcal{F} \tag{4.3}$$

$$\frac{\partial \mathcal{L}}{\partial q} = 0 = \frac{\partial \mathcal{J}}{\partial q} + \psi^T \frac{\partial \mathcal{F}}{\partial q} \tag{4.4}$$

$$\frac{\partial \mathcal{L}}{\partial b^{(m)}} = 0 = \frac{\partial \mathcal{J}}{\partial b^{(m)}} + \lambda^{(m)T} \frac{\partial \mathcal{M}^{(m)}}{\partial b^{(m)}} + \psi^T \frac{\partial \mathcal{F}}{\partial b^{(m)}} \tag{4.5}$$

$$\frac{\partial \mathcal{L}}{\partial b^{(i)}} = 0 = \lambda^{(i)T} \frac{\partial \mathcal{M}^{(i)}}{\partial b^{(i)}} + \lambda^{(i+1)T} \frac{\partial \mathcal{M}^{(i+1)}}{\partial b^{(i)}}, \quad i \in \{m-1, m-2, ..., 1\} \tag{4.6}$$

$$\frac{\partial \mathcal{L}}{\partial v} = 0 = \frac{\partial \mathcal{J}}{\partial v} + \sum_{i=1}^{m} \left(\lambda^{(i)T} \frac{\partial \mathcal{M}^{(i)}}{\partial b^{(i)}} \frac{\partial b^{(i)}}{\partial v} \right) + \psi^T \frac{\partial \mathcal{F}}{\partial v} \tag{4.7}$$

These KKT conditions are driven to zero using a sequential approach, which is deemed more appropriate than a one-shot approach for multipoint optimizations, such as those carried out in this project. The following are the steps involved in this sequential approach:

1. Given the design variables, v, the control mesh is determined via Equation 4.2 and then the mesh is generated.

2. Using these results, Equation 4.3, the flow equations, are solved to obtain the flow variables, q.

3. Equations 4.4 to 4.6 are then solved in the order given to obtain $\lambda^{(i)}$ and ψ, the mesh and flow adjoint variables, respectively.

4. Since all entries of the gradient of the Lagrangian except $\frac{\partial \mathcal{L}}{\partial v}$ are set to zero (i.e. the KKT conditions are satisfied for Equations 4.2 to 4.6), this remaining component is used by the optimizer to find a local minimum.

The cost of this adjoint-based gradient evaluation is nearly independent of the number of design variables. In addition, this discrete-adjoint approach ensures an exact gradient of the discrete objective function, further ensuring compatibility with nonlinear optimization algorithms such that the optimization process can converge fully [14].

4.3 Sequential Quadratic Programming Algorithm

This optimization algorithm essentially obtains the next iterate in the process by modelling the optimization problem at the current iterate by a quadratic programming subproblem [35, 45]. For the optimizations presented in this thesis, SNOPT [15] is used to carry out the optimization and tie the above components together. Both linear and nonlinear constraints, described in Section 4.4.1, are used with this optimizer.

4.4 Optimization Study Overview

For the single-point optimizations of the BWB configuration carried out as part of this thesis, various constraint definitions and additional features have been implemented, as detailed below. A multi-point optimization functionality has also been implemented for use in conjunction with SNOPT. Details of this are summarized in Appendix B.

4.4.1 Constraints

As part of the optimization process, both linear and nonlinear constraints are included to meet the basic design requirements (e.g. internal volume) and to constrain the design variables and, in some cases, couple them in specific manners (e.g. control points on a specific patch edge might be coupled for a linear sweep constraint). Two types of optimizations, planform optimization and varying section optimization, were carried out, as detailed in the subsequent chapter. The following groups and summarizes the various constraints that were utilized or implemented for each of these optimizations. In this summary, the x-coordinate is in the streamwise direction, y-coordinate in the spanwise direction and the z-coordinate follows from the right-hand rule.

Common Constraints

The following are common constraints between the two types of optimizations.

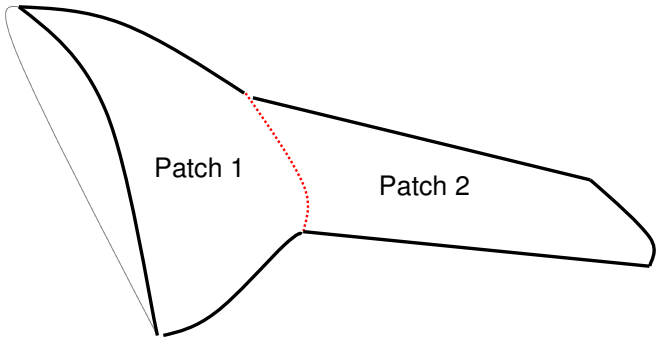

Figure 4.1: Top surface BWB patch definition.

General Restriction Of Control Points In general, all control points can be specified to have varying degrees of freedom. The aerodynamic surface can be decomposed into multiple patches and stitches. Patches define B-spline tensor product surfaces based on the control points and are essentially a specified side of a block which defines the aerodynamic surface of the geometry. Stitches define how these patches are joined and connected at their edges. For instance, Figure 4.1 shows the top surface of the BWB configuration consisting of two patches. The bottom surface is defined similarly. An example of a stitch between the two patches is highlighted in red. All the outer edges of each patch are also considered stitches. Based on this, varying degrees of freedom can be specified for specific stitches and patches, thus enabling a general definition of the degrees of freedom of a set of control points. For instance, this definition can be used to constrain the leading or trailing edges to specific degrees of freedom. Note that the span is fixed for these optimizations through this type of restriction.

Lift Constraint For this nonlinear constraint, the target lift coefficient is actually defined as $C_L S^*$, where C_L is the lift coefficient and S^* is the non-dimensionalized area. Details of how to determine this value are provided in Appendix C.

Planform Area In order to constrain the lift coefficient, the planform area (or another consistent reference area) must be constrained in addition to the lift. In the cases presented in this thesis, the initial value of the planform area is used as the target value for this nonlinear equality constraint.

Symmetry Edge This constraint forces control points at the symmetry plane and those just off the symmetry plane to have the same x- and z- values, effectively ensuring that this portion of the surface is perpendicular to the symmetry plane. This linear, equality constraint is enforced everywhere along the root-chord of the BWB.

Linear Sweep Linear sweep constraints couple the x- and y-coordinates of the leading edge or trailing edge control points. Though not necessary, they are used on the varying section optimization primarily to limit the freedom.

Linear Dihedral In a similar manner, linear dihedral constraints couple the y- and z-coordinates of the leading edge or trailing edge control points. Again, for increased freedom and a more interesting problem, these constraints can be excluded with varying sections.

Planform Optimization Constraints

Fixed Airfoil Section The x- and z-coordinates of the control points along an airfoil section are constrained such that their x- and z-positions relative to the leading edge control point are maintained at constant ratios to the chord, effectively fixing the airfoil section during the optimization process.

y-position Constraints With the use of fixed airfoil sections, the control points on the main body are maintained at specific spanwise locations using this constraint in order to ensure specific thickness-to-chord ratios at these points. This, in turn, maintains the required space for internal volumes and removes the need for a volume constraint.

Chord-length Constraints Minimum chord-length constraints maintain an approximate chord-length on the specific sections where applied. This helps ensure sufficient internal volume by maintaining a minimum thickness-to-chord ratio when coupled with the fixed airfoil section constraint. Note that these constraints are implemented using the control points; stricter constraints would instead use the aerodynamic surface grid nodes directly, providing an exact evaluation of the chord-length(s).

Varying Section Optimization Constraints

Volume The volume of the entire blended-wing-body may also be constrained. For optimizations with fixed airfoil sections, this nonlinear, inequality constraint was not enforced or necessary; however, to ensure sufficient volume for fuel, passengers, and structural components and to prevent the optimizer from reducing the shape to a flat plate, volume constraints are employed for optimizations involving varying sections.

Specific Volume This constraint is an alternative option to that above. In this case, the aircraft is treated as if it consists of two separate volumes — specifically, the main body and the outer wing, enabling control over the volume specific to each section, as defined by the patch definition. This constraint is also an inequality constraint.

x-coordinate Ratio This linear equality constraint maintains the x-coordinates relative to the leading edge at constant ratios to the chord-length.

Colinearity In order to enforce continuity between patches, this constraint was implemented. In Figure 4.2, the leading edge of a portion of the wing is considered along with three of the control points at a given spanwise station. Points A, B, and C are forced to be colinear by maintaining the vector defined by B and C parallel to the

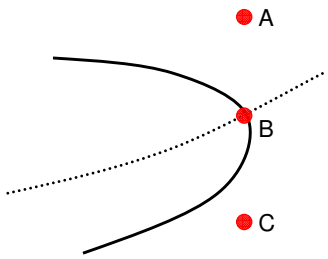

Figure 4.2: Along the leading edge, the three control points are forced to be colinear to enforce continuity.

vector defined by A and C. The constraint is not only applied at the leading edge but also on stitches between patches, such as that highlighted in red in Figure 4.1. An additional constraint for the x-coordinates of the points along the leading edge is included in conjunction with this constraint to maintain the two vectors at right angles with the x-axis. This helps ensure the mesh along the leading edge does not warp, causing the mesh movement to fail.

y-coordinate Ratio This linear equality constraint maintains the the y-coordinates relative to the root at constant ratios to the total span. Though the span is fixed for the optimizations in this thesis, this constraint would accommodate a situation in which span variations are allowed.

Main Body Thickness These nonlinear inequality thickness constraints are defined using the aerodynamic surface grid nodes. Based on the polyhedron location in the baseline geometry, target thickness values can be specified at specific x,y-positions.

Main Body Height This constraint is similar to that above, but enables the user to specify a target height above and/or below the xy-plane at specific x,y-positions, ensuring that the fuselage portion of the main body does not warp significantly and thus easily accommodates the polyhedron. Note that the thickness constraints are unnecessary if height constraints both above and below the xy-plane are enforced.

Crossover Prevention Constraints This constraint requires that the difference between control points on the upper and lower surfaces is always greater than zero, preventing crossover of the surfaces. The volume constraints will not prevent crossover, making this constraint — or some variation of it — an important one. This constraint also allows far more freedom than the two subsequent constraints described below.

Thickness (Control Point) This constraint is intended to limit the freedom of the control points by allowing the thickness to vary within a user-specified percentage of the original thickness [4] It also effectively helps prevent cross-over of surfaces; as such, if it is used, the above constraint would not be necessary. Note that this is different from the main body thickness constraint above since it is based on the control points directly, whereas the main body thickness constraints are based on the surface grid nodes.

Height (Control Point) Similar to the above constraint, this also limits the freedom of the control points by allowing the height of a given control point above the chordline to vary within a user-specified percentage of the original height [4].

Leading and Trailing Edge z-bound This constraint places a bound on the z-coordinates of the main body leading and trailing edges, limiting the freedom and preventing warping, especially at the fuselage portion of the main body.

Linear Tip This linear equality constraint maintains a linear tip on the outer wing to prevent warping on this portion of the geometry. Note that this constraint works in conjunction with the x-coordinate ratio constraint above. Otherwise, a nonlinear version of the constraint would be necessary to account for additional dependencies.

Tip Chord-length In order to prevent the tip chord-length from decreasing drastically, to the point where the mesh quality deteriorates considerably, a minimum

chordlength constraint is implemented.

4.4.2 Additional Features

The following capabilities were also added as part of this thesis for analysis purposes and to help ensure convergence, if necessary.

Drag Divergence Plot

Drag divergence plots are useful in better understanding the degree to which an optimization has improved a given shape. In general, one would expect the drag divergence Mach number to increase after an optimization. To quickly obtain drag divergence plots, single-point optimizations over a user-specified range of Mach numbers with a single design variable (angle of attack) and constraint (lift target) are carried out.

Remesh Capability

In the case where the quality of the mesh for a given geometry deteriorates over the course of an optimization to the point where it actually hinders the optimization process, a remesh of the most current geometry may be necessary. As such, an optional feature allowing the user to output files at each iteration of the optimization process was added. These files contain the relevant information about the B-spline definition of the geometry. Using code external to the flow-solve/optimization package, a new geometry file can be generated to be used in the remeshing process.

Chapter 5

Results

Two types of single-point optimizations are carried out: planform optimizations with fixed airfoil sections and optimizations with varying airfoil sections.

5.1 Planform Optimization

5.1.1 Optimization Problem Description

For the optimization, the geometry is parameterized such that it consists of two sections: the main body and the outer wing. Extending this to include more sections for more complex BWB geometries (to investigate winglets, C-wing geometries, etc. for instance) would be straightforward. The design variables consist of the B-spline control point coordinates in the x- and z-directions and the angle of attack, depending on the case; however, the constraints outlined below couple the control points, effectively limiting their freedom and reducing the actual number of design variables.

The airfoil sections are maintained on the entire shape through constraints which scale the airfoils as the chord length varies. These airfoil sections are two personally modified versions of a supercritical airfoil, sc20414 [72]: on both, the blunt tip at the trailing edge, which is typical of supercritical airfoils, has been removed, and the camber is also slightly modified to ease both the geometry generation and the meshing process.

Geometry	C_D	Drag Reduction
Baseline	0.02720	-
Elliptical induced drag	0.01280	-
A	0.01837	32.5%
B	0.01783	34.4%
C	0.01667	38.7%

Table 5.1: Drag coefficients and percent drag reductions for baseline and planform optimized geometries.

Both airfoils are shown in Figure 3.3. On the main body, only the trailing edge is free to move. On the outer wing, linear sweep and twist constraints are in place, with the possibility to allow for dihedral as well. Minimum chord length constraints are applied in order to satisfy the internal volume constraints, as are spanwise width constraints. The overall span is fixed, along with the planform area. The lift coefficient is constrained at 0.357, and the objective function is the drag coefficient. Three cases are presented here and other than the following variations, the problem definitions for the three are identical:

Case A Fixed angle of attack of 3 degrees — since aircraft typically fly at angles of attack of 2 to 3 degrees to maintain a reasonable floor angle for passenger comfort.

Case B Fixed angle of attack of 3 degrees with optional dihedral on the outer wing active. This is the only case in which dihedral was active.

Case C Free angle of attack with no upper or lower bounds.

5.1.2 Optimization Results

The resulting geometries are shown in Figures 5.1, 5.2, and 5.3. Case B geometry varies from both Cases A and C with its lower taper ratio and positive dihedral. The effect of the addition of positive dihedral might be considered similar to the effect of non-planar surfaces such as winglets. The key differences between the two geometries of Case A and Case C include higher sweep and twist (washout) on the Case C geometry.

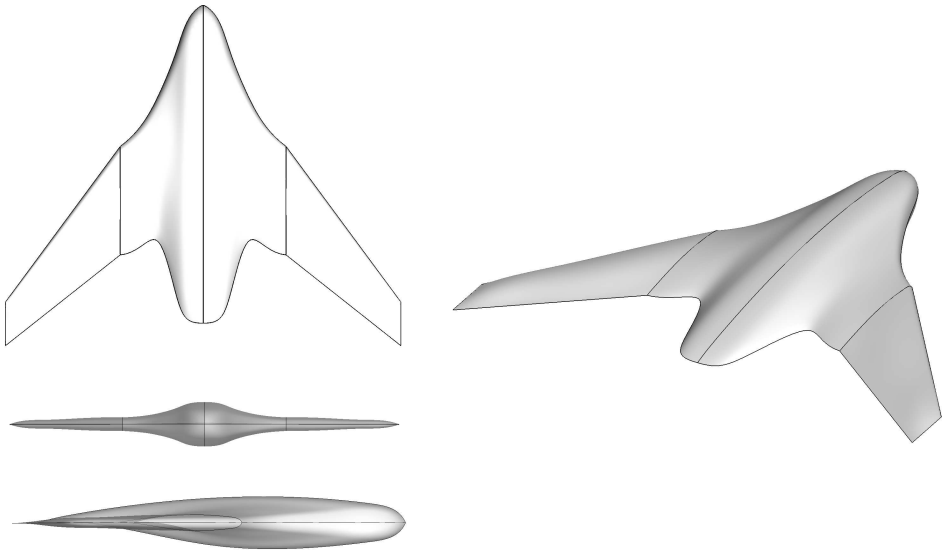

Figure 5.1: Various views of the optimized BWB geometry for Case A.

Table 5.1 compares the C_D values for the baseline geometry and the three optimized geometries. From this table, we can see that the Case C geometry results in the lowest drag by a reduction of almost 39% relative to the baseline geometry. However, this additional reduction in drag comes with an increased angle of attack of 4.43 degrees relative to the 3 degrees for both Case A and B. Comparing these drag values to that for the elliptical induced drag, determined using the target C_L value and the aspect ratio of 3.17 (Chapter 2), the room for improvement is evident.

The four sub-figures in Figure 5.4 show the spanwise lift distributions on the baseline and optimized geometries, compared to elliptical lift distributions. The baseline distribution is far from the elliptical lift distribution. Apart from the main body, the Case A distribution is closer to the elliptical distribution. However, the Case B distribution over the same outer wing portion is moving away from this elliptical distribution. Case C moves further away from it and appears to be tending towards a more triangular/elliptical lift distribution. The fact that this distribution on the Case C geometry leads to the lowest drag is in agreement with results found by Qin *et al.* [53]: in the case where shocks cannot be eliminated completely, an elliptical lift distribution can no longer

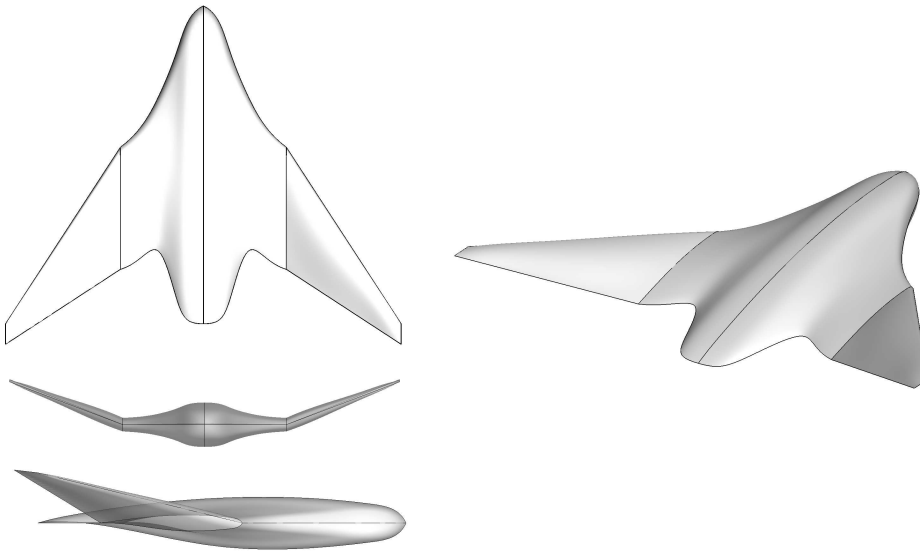

Figure 5.2: Various views of the optimized BWB geometry for Case B.

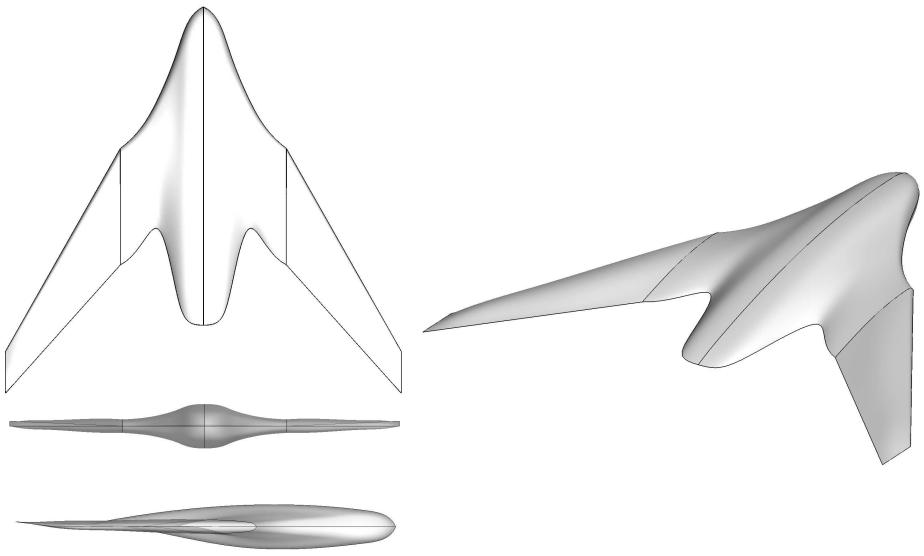

Figure 5.3: Various views of the optimized BWB geometry for Case C.

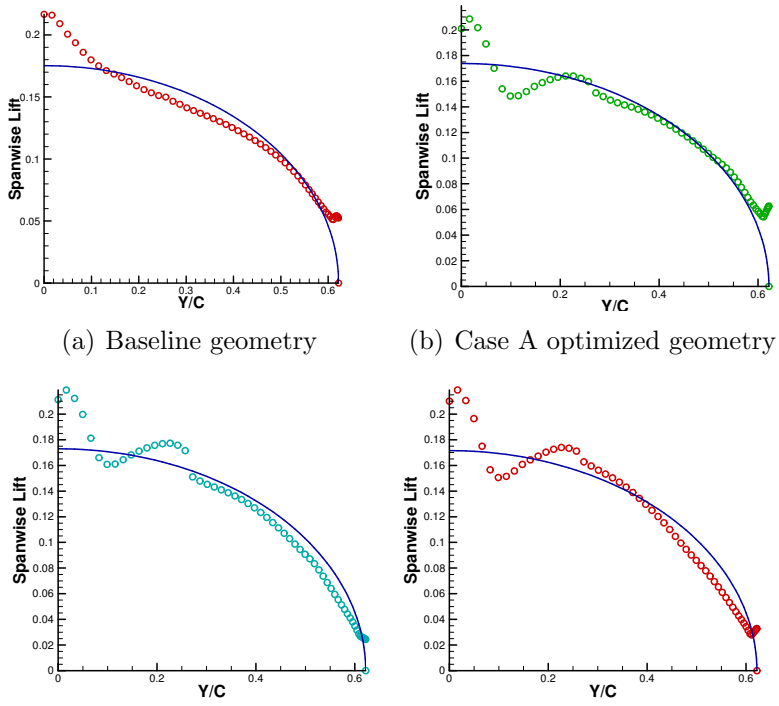

(a) Baseline geometry (b) Case A optimized geometry

(c) Case B optimized geometry (d) Case C optimized geometry

Figure 5.4: Spanwise load distributions

be the goal for minimum drag design, as a compromise between wave drag due to shock wave formation at transonic speeds and induced drag due to lift is required.

Figures 5.5, 5.7, and 5.9 show pressure coefficient plots for the optimized geometries for Cases A, B, and C at the target lift coefficient of 0.357 and the same spanwise locations as on the baseline geometry (Figure 3.3). For Cases A and B, multiple shocks of significant strength are present on the geometry at the spanwise locations shown. However, for Case C, a sharp shock is still present on the top surface, though not as strong as that on the baseline geometry. In addition, the shock is primarily present along the outer wing leading edge. Despite the drag reduction, the maximum local Mach number on the top surface of this optimized geometry is quite high - approximately 2.44 (Figure 5.10).

From the pressure coefficient plots, the main body portions of the Case A and Case B geometries also appear to be generating negative lift over small portions, which would

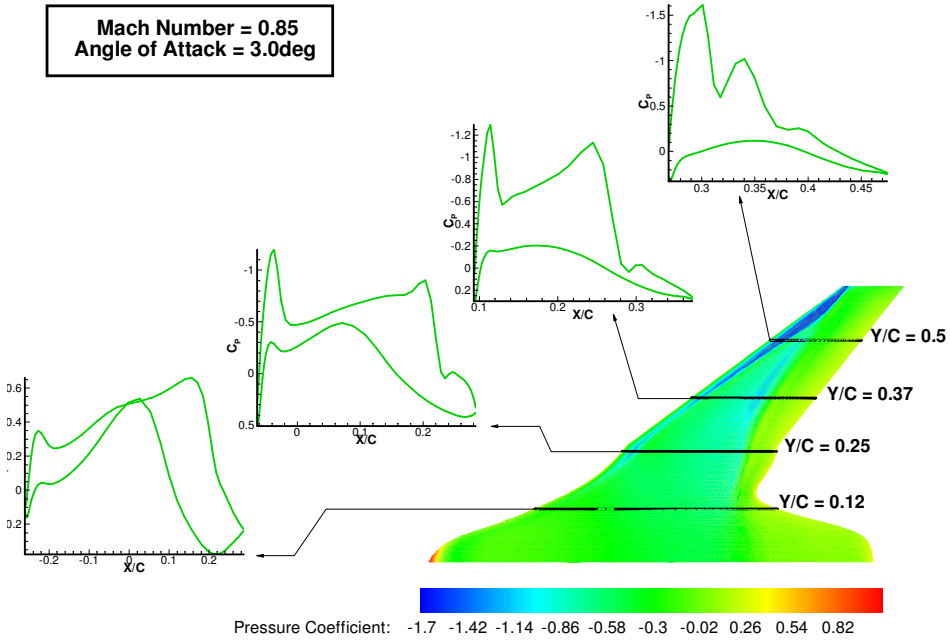

Figure 5.5: Pressure coefficient distribution over the top surface of the optimized BWB geometry (Case A) and at indicated spanwise locations.

be undesirable; however, this does not appear to be an issue for the Case C geometry.

Taking a closer look at the drag polars of the baseline geometry and the three optimized geometries (Figure 5.11), we see that all three have improved performance over the range of lift coefficients shown, not just at the design point. Though Case C has the lowest drag in the vicinity of the target lift coefficient, it has the highest drag of the optimized geometries for lower lift coefficients. It is also important to remember that the target lift and higher lift values are obtained at much higher angles of attack for Case C than for Cases A and B.

Figures 5.12, 5.13, and 5.14 show the convergence histories for the three cases considered. Here feasibility refers to the nonlinear constraint violation. The user-specified tolerances for both feasibility and optimality are 10^{-6}. Each function evaluation represents a successful iteration in the optimization process.

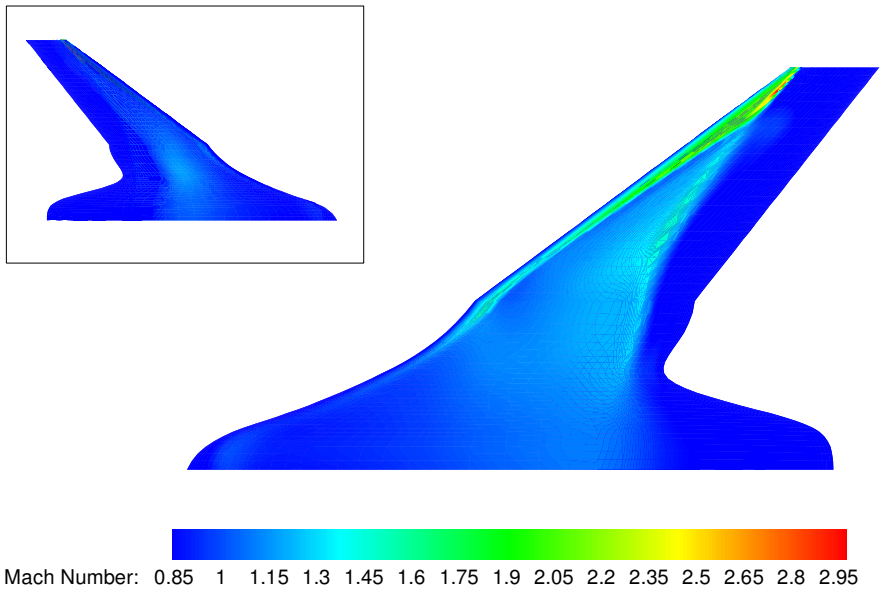

Figure 5.6: Mach number distribution over the top and bottom (inset) surfaces of the optimized BWB geometry (Case A).

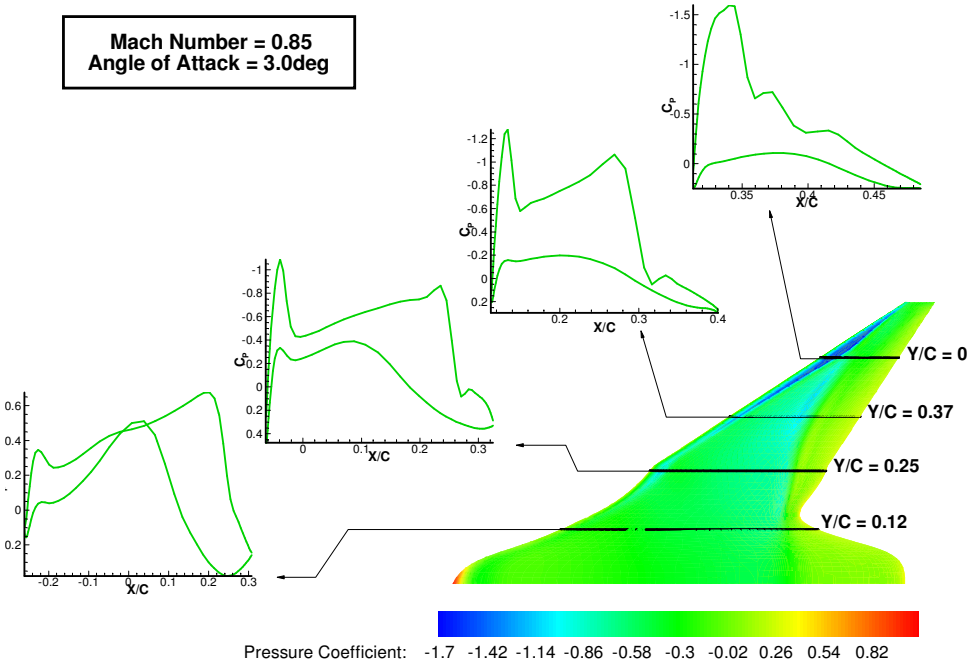

Figure 5.7: Pressure coefficient distribution over the top surface of the optimized BWB geometry (Case B) and at indicated spanwise locations.

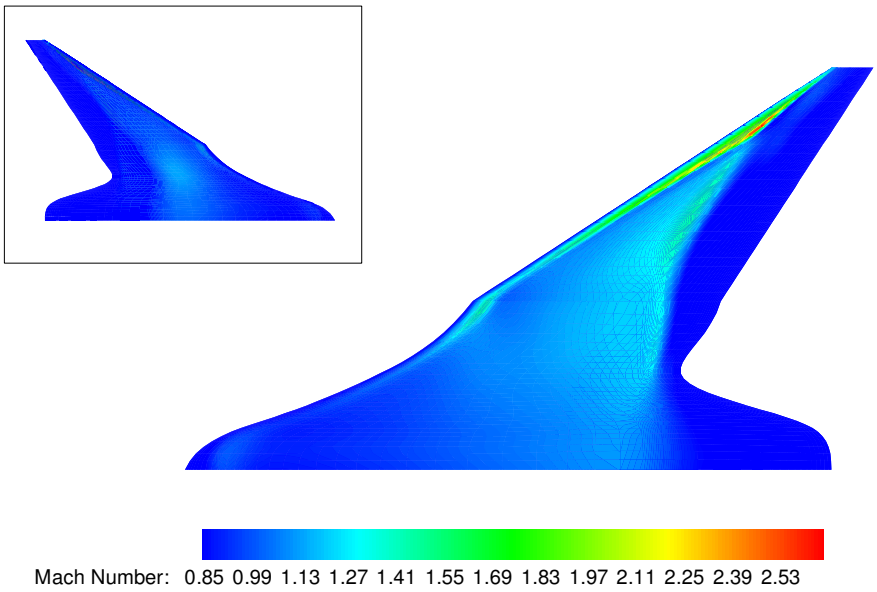

Figure 5.8: Mach number distribution over the top and bottom (inset) surfaces of the optimized BWB geometry (Case B).

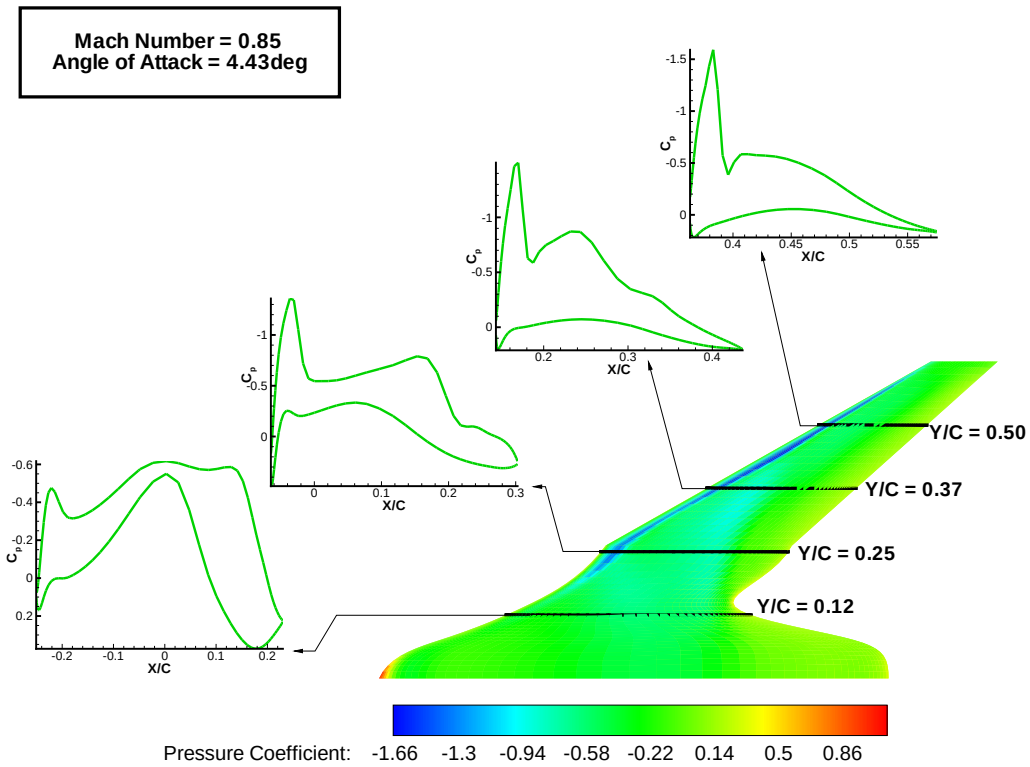

Figure 5.9: Pressure coefficient distribution over the top surface of the optimized BWB geometry (Case C) and at indicated spanwise locations.

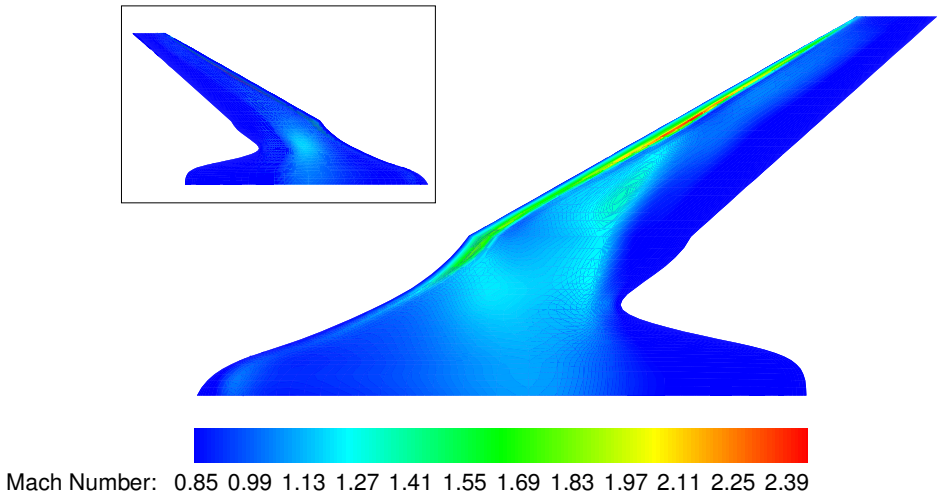

Figure 5.10: Mach number distribution over the top and bottom (inset) surfaces of the optimized BWB geometry (Case C).

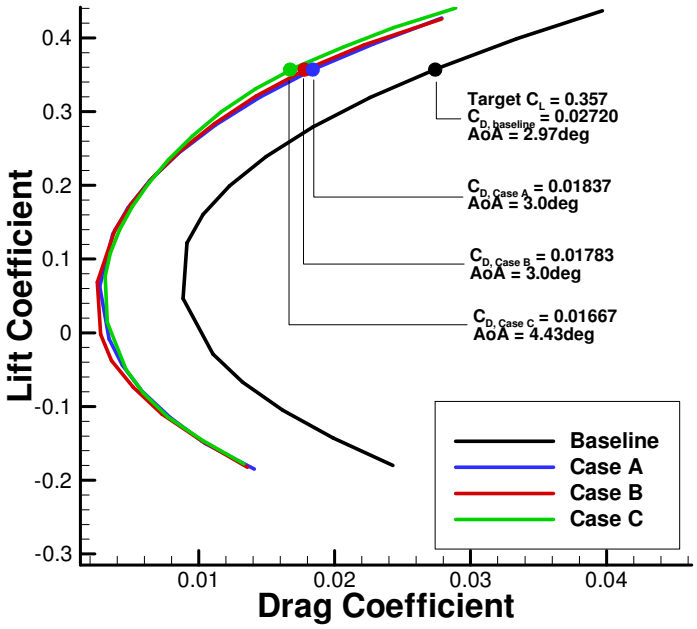

Figure 5.11: Comparison of the drag polars of the baseline and optimized BWB geometries.

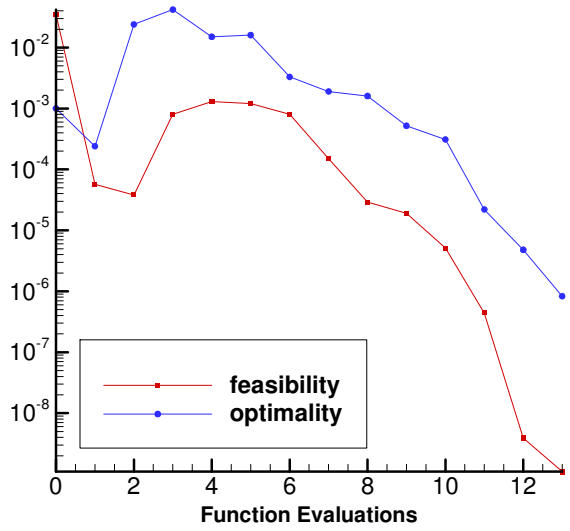

Figure 5.12: Convergence history for Case A.

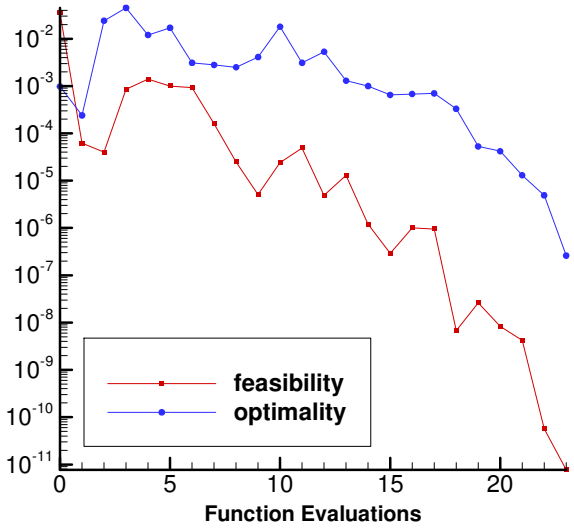

Figure 5.13: Convergence history for Case B.

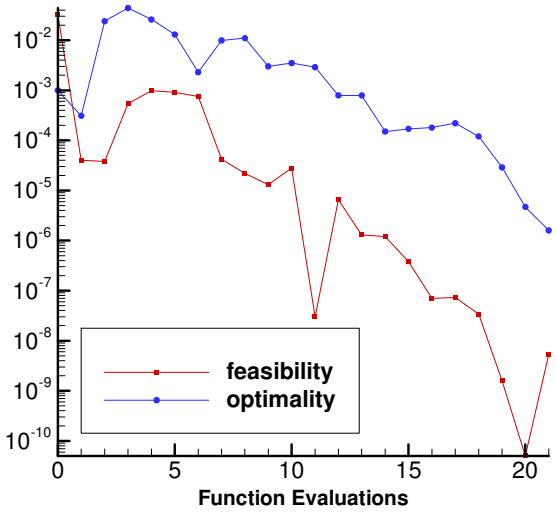

Figure 5.14: Convergence history for Case C.

5.2 Varying Sections

For the varying section optimizations, two different cases were carried out with a different set of constraints: Cases D and E. Similarities between these optimizations and the planform optimizations include the baseline geometry and the geometry parameterization, which consists of two sections — the main body and the outer wing. In addition, the planform area and span are fixed. The same C_L constraint is specified, and the objective function is the drag coefficient. The angle of attack is included as a design variable.

Between the two cases, the following are the common constraints: The main body and outer wing sections of the BWB each have a specific volume constraint. Colinearity constraints help ensure C^1 continuity at the leading edge and between the two sections.

5.2.1 Case D: Optimization Problem Description

For Case D, the x-coordinates are maintained at the same chordwise location relative to the leading edge. Similarly, the y coordinates are maintained at their spanwise locations relative to the symmetry plane. Since the span of the BWB is fixed, the y-coordinates are effectively also fixed. The z-coordinates are controlled using the thickness and height constraints described earlier for control points. The points are allowed to move within

$\pm 50\%$ of their original thickness and height values using these constraints. In order to ensure sufficient internal volume, height constraints are included for the upper and lower surfaces. The z-coordinates of leading and trailing edge points are also limited by the leading and trailing edge bound constraints. Finally, both edges have linear sweep and dihedral constraints in place.

5.2.2 Case E: Optimization Problem Description

For this problem, x- and z-coordinates of the control points are now design variables. Again, the optimizer can modify the spanwise section shapes. The span is effectively constrained because the y-coordinates are held fixed. Crossover prevention constraints ensure the surfaces do not intersect and cross over each other. Finally, minimum thickness constraints — rather than the height constraints employed in Case D — are included to ensure the outer shell envelops the internal volume polyhedron. Overall, this case has the most freedom of all the cases presented.

5.2.3 Optimization Results

Case D converged successfully. Case E was feasible in the sense that all the constraints were satisfied; however, the target optimality tolerance was not achieved, i.e. the optimization did not converge fully. The resulting geometries are shown in Figures 5.15 and 5.16. The twist distribution is evident from the front and rear views of the optimized geometries. At this Mach number, one would expect a shock-free flow. This is achieved for Case D but not Case E. As can be seen in Case D, this can be achieved by adding some sweep, but the lack of convergence of the optimizer appears to have prevented this on Case E.

Table 5.2 compares the C_D values for baseline geometry, the three planform optimization geometries and the two section-optimized geometries. Case E, despite the presence of a shock, has the most significant drag reduction, with Case D close behind. At one degree, the angle of attack for the Case E geometry is also the lowest of all shapes

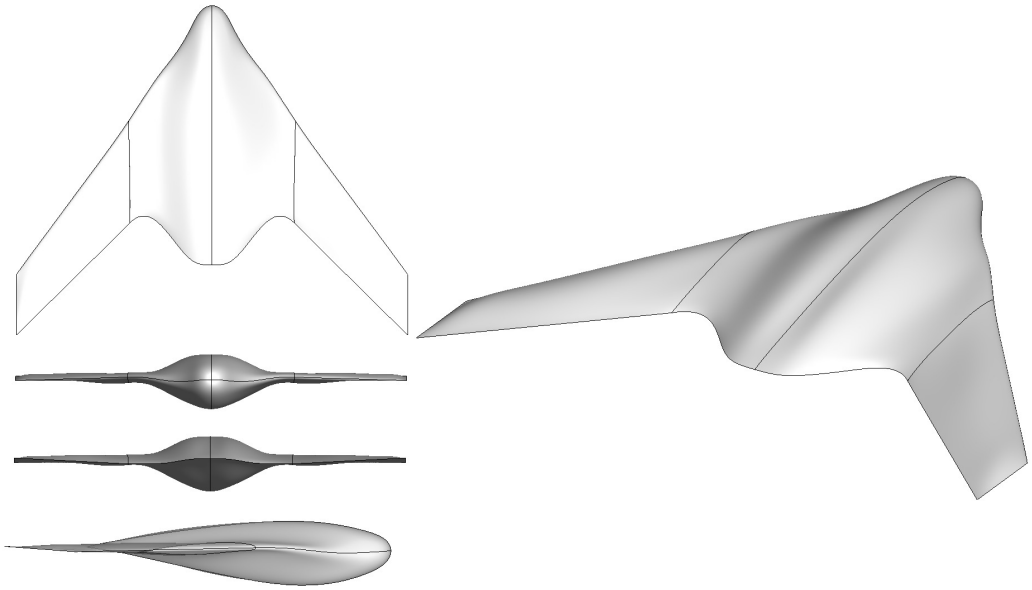

Figure 5.15: Various views of the Case D section-optimized BWB geometry.

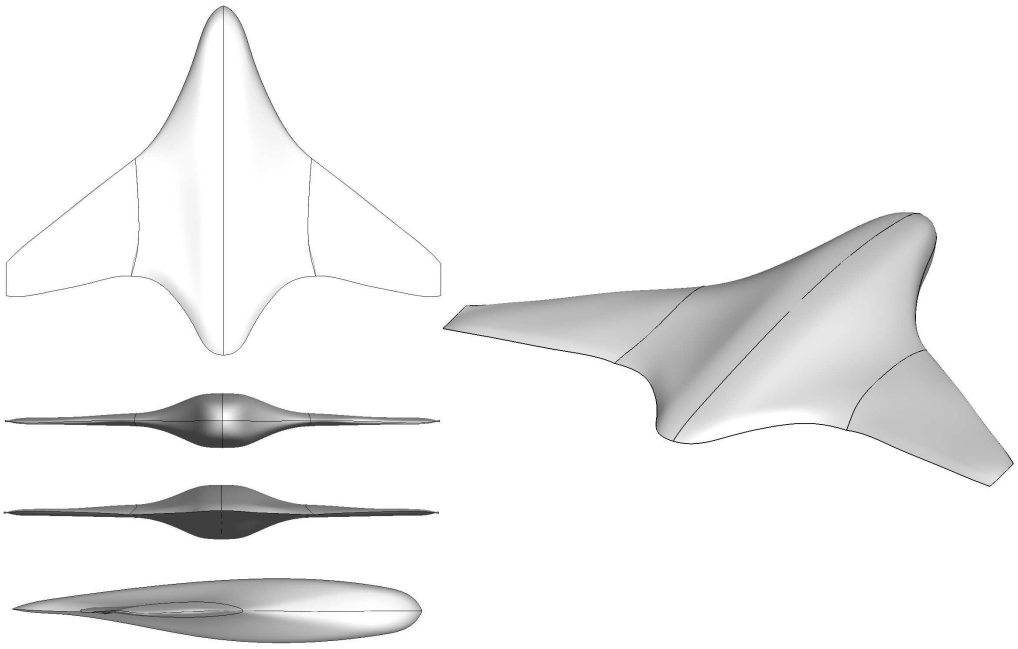

Figure 5.16: Various views of the Case E section-optimized BWB geometry.

	Geometry	C_D	Drag Reduction
	Baseline	0.02720	-
	Elliptical induced drag	0.01280	-
Planform Optimization	A	0.01837	32.5%
	B	0.01783	34.4%
	C	0.01667	38.7%
Section Optimization	D	0.01351	50.3%
	E	0.01313	51.7%

Table 5.2: Drag coefficients and percent drag reductions for baseline and all optimized geometries.

considered, including the baseline geometry.

Figure 5.17 and 5.18 show pressure coefficient plots for the two section-optimized geometries at the target lift coefficient of 0.357 and the same spanwise locations as on the baseline geometry (Figure 3.3). Profiles of the optimized airfoils at these spanwise locations are also included. Despite the significant drag reduction and varying sections of this optimization, a very weak shock still exists towards the rear portion of the wing on the Case E geometry as can be seen in Figure 5.20. However, for Case D (Figure 5.19), this shock has been eliminated.

Figure 5.21 shows the spanwise lift distributions on the optimized geometries and the baseline geometry, compared to elliptical lift distributions. The distribution of the Case E geometry is the closest to the elliptical distribution of all the shapes presented. For Case D, this indicates that although the wave drag was eliminated through elimination of the shock, the induced drag is still greater than it appears to be for Case E. That said, the wave drag has been largely eliminated for Case E as well, given the additional fact that the C_D for Case E is fairly close to the elliptical induced drag and zero wave drag C_D. It is not clear, however, how the sections of this geometry would perform in a turbulent flow analysis.

Convergence histories for the two cases are shown in Figures 5.22 and 5.23. Again, feasibility refers to the nonlinear constraint violation, and each function evaluation represents a successful iteration in the optimization process.

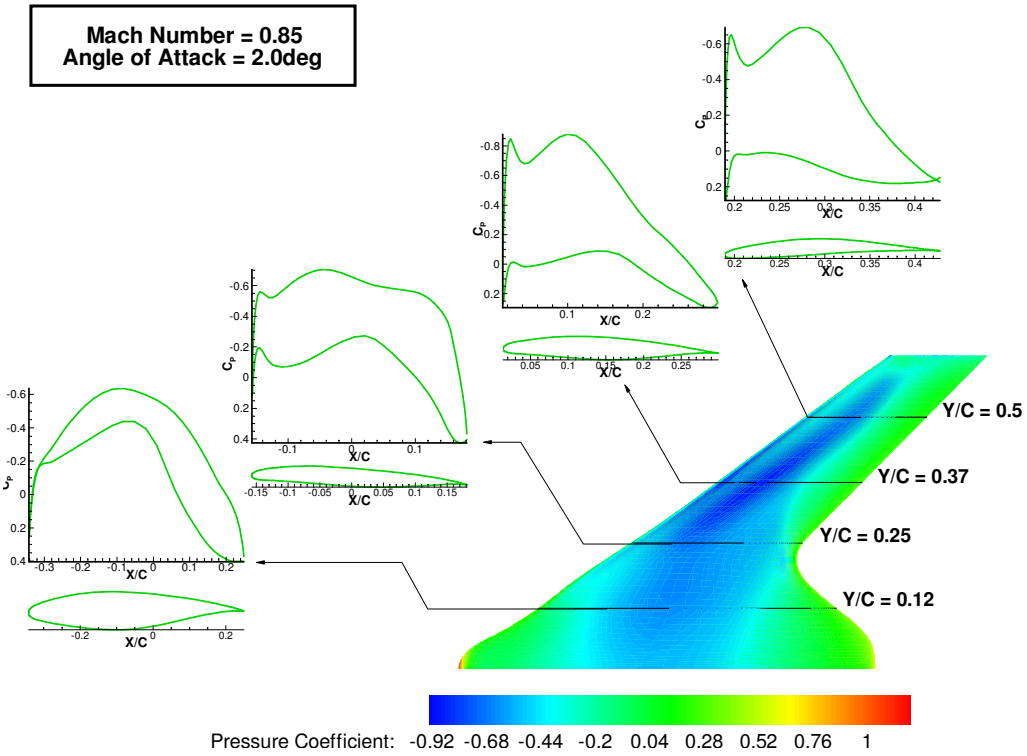

Figure 5.17: Pressure coefficient distribution over the top surface of the section-optimized BWB geometry (Case D) and at indicated spanwise locations.

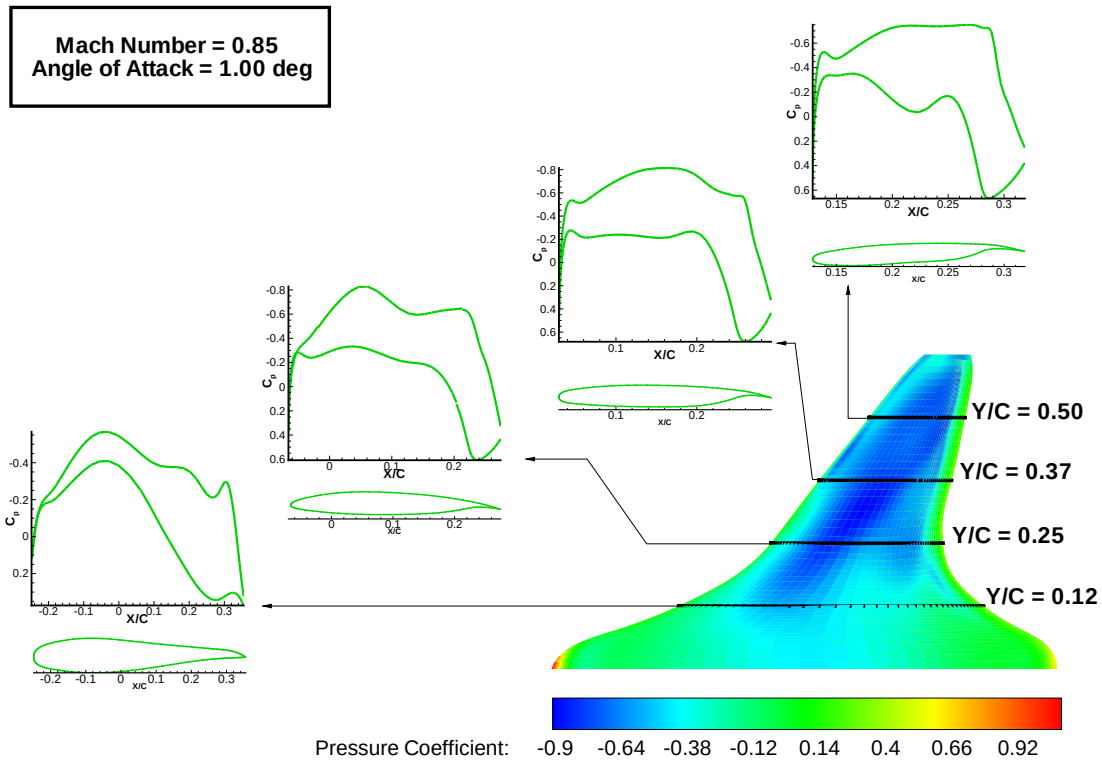

Figure 5.18: Pressure coefficient distribution over the top surface of the section-optimized BWB geometry (Case E) and at indicated spanwise locations.

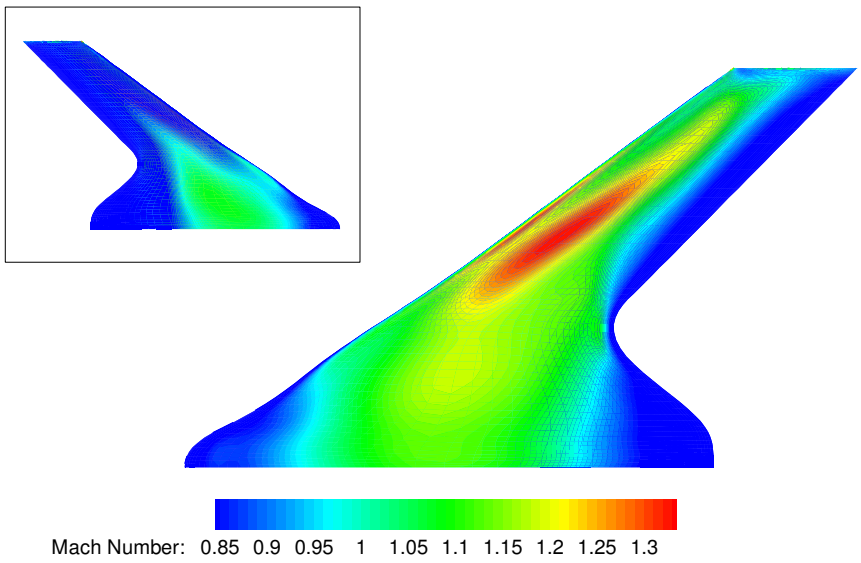

Figure 5.19: Mach number distribution over the top and bottom (inset) surfaces of the section-optimized BWB geometry (Case D).

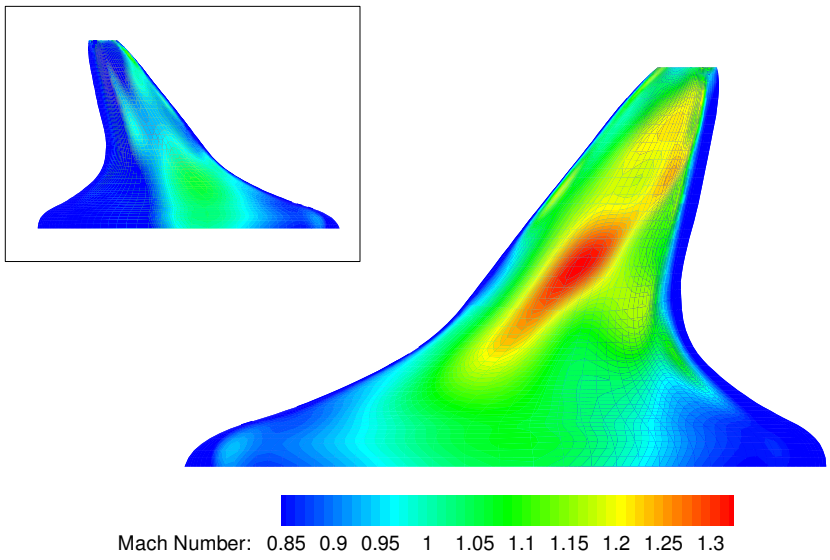

Figure 5.20: Mach number distribution over the top and bottom (inset) surfaces of the section-optimized BWB geometry (Case E).

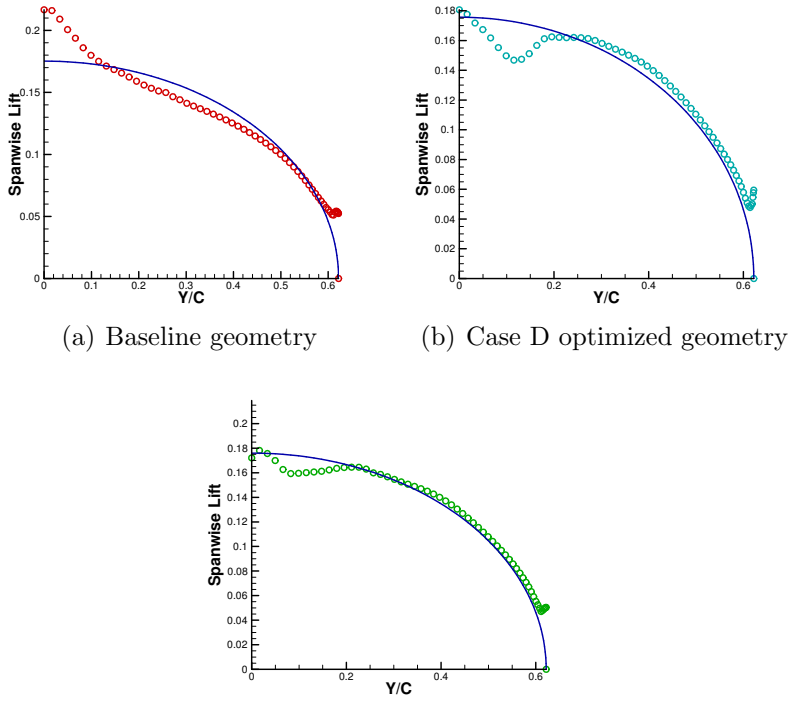

(a) Baseline geometry

(b) Case D optimized geometry

(c) Case E optimized geometry

Figure 5.21: Spanwise load distributions

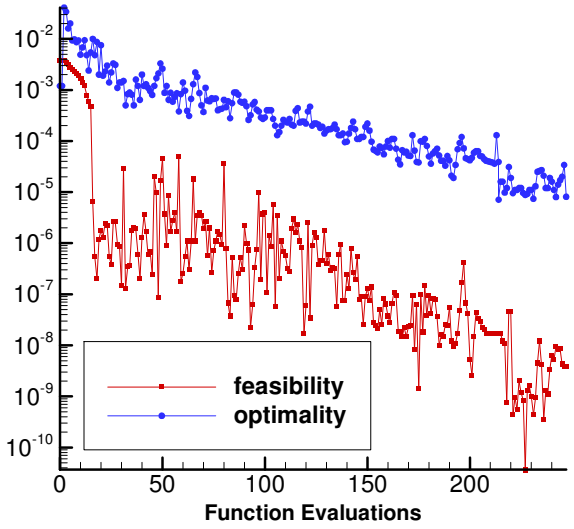

Figure 5.22: Convergence history for Case D.

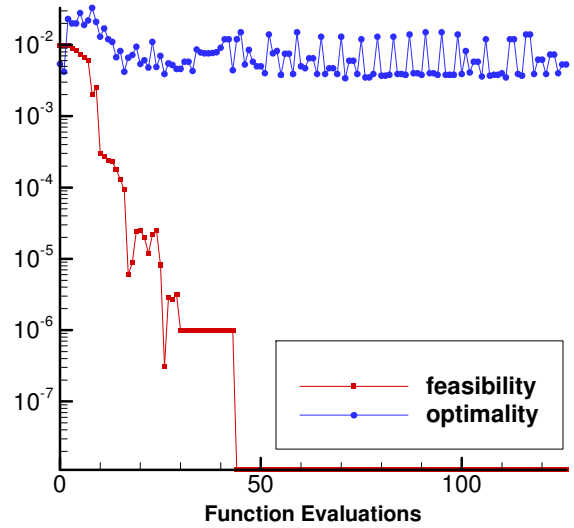

Figure 5.23: Convergence history for Case E.

Chapter 6

Conclusions and Recommendations

The blended-wing-body configuration is an alternative aircraft configuration that has potential to be a viable and advantageous option in comparison with current conventional aircraft. The results of the inviscid optimization of this configuration in this thesis have shown significant drag reduction between the baseline geometry and final optimized geometry. A single-point, transonic optimization with limited freedom and fixed sections resulted in up to 38.7% induced and wave drag reduction relative to the baseline: for the target C_L of 0.357, a C_D of 0.01667 is achieved, resulting in an inviscid lift-to-drag ratio of 21.4. With increased flexibility and varying sections, drag reduction of 51.7% was achieved: the C_D is reduced to 0.01313 and the inviscid lift-to-drag ratio increased to 27.2. Of course, a comparison with conventional aircraft is necessary in order to gain an understanding of the true value of these BWB designs.

There are several aspects of the project that would be of interest for future work. The first and most obvious direction is to incorporate viscous effects with the Reynolds-Averaged Navier Stokes equations.

Optimizations with higher Mach numbers could also be carried out; however, a linearization of the pressure switch in the flow solver would be necessary to avoid the error introduced through the use of second-difference dissipation.

Multi-point optimizations (Appendix B) and specific studies focused on wave drag control mechanisms such as the 3-dimensional control bumps studied by Qin *et al.* [78] and passive laminar flow control via wing shaping might also be of interest.

The BWB is also a highly integrated configuration and as pointed out by Kroo [76], is an 'arena rich in opportunities for MDO'. As such, incorporating structural effects (Appendix A) and ultimately doing MDO on this configuration is preferable, with the potential to use the optimized shapes presented in this thesis as initial geometries. As part of this study, given the suitability of the BWB configuration for larger aircraft, the Large Aircraft for Short Ranges (LASR) concept studied by Kenway *et al.* [24] could also be applied to the BWB to determine how much more of an advantage it might give over existing conventional aircraft and a conventional LASR-type aircraft.

With respect to the tools being used, a parallelization of the mesh movement algorithm presented by Truong *et al.* [71] might prove to be faster and more robust than the current integrated approach. Incorporation of a measure of mesh quality into a constraint or objective function — in order to ensure a certain level of quality is always maintained during an optimization — might also help reduce the number of mesh movement and flow solve failures during the optimization process; however, this would also likely reduce the freedom of the optimization process and would require a study of the most appropriate measure of mesh quality. Finally, by eliminating the learning curve required of users of current mesh generation software, an alternative, automated mesh generation process might better help address this issue.

With respect to the baseline geometry, in the case where the dependence on initial geometry has not been eliminated, C-wing BWB geometries or BWB geometries with winglets will be of interest. This would require the inclusion of more than the two sections utilized for this thesis. Constraints developed as part of this work would also have to be extended to accommodate these additions. In order to obtain an improved baseline, as opposed to the relatively arbitrary geometry adopted in this work, 2-dimensional opti-

mizations on the airfoils can be carried out and then projected back to the 3-dimensional shape; however, as Qin *et al.* [53] point out in their work, this clearly does not account for the 3-dimensional effects. Finally, a more generalized geometry parameterization which enables the generation of a range of conventional and unconventional geometries could be developed. Ultimately, however any dependence on the initial geometry should ideally be eliminated.

As part of the optimization problem definition, rather than employing fixed internal volume constraints (via height or thickness constraints), incorporating a more fluid volume constraint would increase the flexibility of the optimization. That is, for each iteration in the optimization process, a constraint can be used to ensure sufficient space for the given payload, while allowing for new and unique seating configurations as the outer aerodynamic geometry evolves. In addition, while keeping the overall span fixed, allowing limited freedom of the control points between the symmetry section and wing tip in the spanwise direction would also increase flexibility, while better enabling the optimizer to take advantage of the 3-dimensional effects inherent on a BWB.

A simple yet interesting study might also involve a BWB optimization with a fixed volume constraint for higher transonic speeds. The optimized geometry's cross-sectional area distribution should be similar to that for the Sears-Haack body, as found by Liebeck [29].

Appendices

Appendix A

Aerostructural Considerations

A.1 Motivation

Incorporating a structural model with aerodynamics is a useful study since these two disciplines are of primary importance in aircraft design. Furthermore, performing a coupled aero-structural optimization is preferable to a sequential optimization, since this not only aids in finding the true optimum, but also allows for larger modifications when including structures in a high-fidelity wing optimization [36].

As pointed out in [64], structural weight and deformations affect aerodynamic design of an aircraft and vice versa. For the structural deformations, a jig-shape approach can be employed so that the structure is constructed such that the structural deformations result in the desired shape. By assuming constant deformations over the majority of the flight mission, the structural deformation impact on the aerodynamic performance is effectively eliminated by the jig shape. This implies that the aerodynamic design is affected only by the structural weight, whereas the aerodynamic design affects all aspects of the structural design. Based on this, an asymmetry exists. With this asymmetry, aerodynamics is treated as the higher level of a two-level optimization problem and an emphasis on improved aerodynamic models arises. Given this, the incorporation of a simple, low-fidelity structural model with a high-fidelity aerodynamic optimization, such

as that considered here, is justified and becomes a topic of great interest from a multi-disciplinary optimization (MDO) perspective. Examples of simple structural models are discussed below.

Taking into consideration the highly integrated nature of the various disciplines — aerodynamics, structures, and controls — in the BWB [52] and the great potential for MDO studies with the BWB [76], this project is an ideal starting point for such a coupled aero-structural optimization.

A.2 Structural Models

Structural models of varying fidelity can be incorporated in an aero-structural optimization. These range from root-bending moment considerations, statistical weight equations, equivalent beam or plate models, to detailed, high-fidelity Finite-Element Models of the structures in an aircraft. A summary of the methodologies for interfacing between Euler/Navier-Stokes equations and structural models of varying fidelity, along with the advantages and disadvantages of these various methodologies can be found in [16].

Two feasible options for a low-fidelity model for incorporation with the BWB aerodynamic shape optimization were found during the course of this thesis work:

- Weight equations based on BWB studies [2]
- Equivalent beam and plate models [11, 12, 13, 23]

For the first option, Bradley [2] uses regression analysis to develop weight equations for the fuselage and aft-body, which supports the engines and is located behind the fuselage. This analysis was performed using weight data obtained from equivalent plate models for various BWB models ranging from 250 to 450 passenger aircraft. These equations are mentioned in Section 2.3 and were used as a means of obtaining a rough weight estimate. As such, the equation used for the wing weight estimation can also be used here. Using these equations at each step in the aerodynamic optimization process, the

structural weight of the BWB can be calculated and used in the Breguet range equation:

$$Range = V\frac{L}{D}I_{sp}\ln\left(\frac{W_i}{W_f}\right) \tag{A.1}$$

where V is the velocity, $\frac{L}{D}$ the lift-to-drag ratio, I_{sp} the specific impulse, W_i the initial weight and W_f the final weight. The equation can be used as the objective function to maximize range or minimize weight of fuel.

However, points of concern with this method exist. First, the large size of the BWBs considered in [2] limits their application. Furthermore, in order to employ these equations, one must find a consistent way to estimate certain parameters of measure necessary for the calculation, such as the taper ratio of the aft-body. This may not always be trivial if the BWB shape diverges significantly from a 'typical' BWB shape, as was found to be the case in the optimizations presented in this thesis. In addition, as pointed out in [64], in the case where multiple design conditions are considered, weight equations are not always suitable. This is certainly a point of concern with extensions of this thesis work since multipoint optimization is of interest.

For the second option, the work in [23] incorporates an equivalent beam model with panel methods to optimize non-planar surfaces. Equivalent beam and plate models essentially model the otherwise complicated structural elements of an actual aircraft structure using either beam or plate elements, respectively, maintaining consistent inertial properties between the models. The Python beam model developed in [23] was selected as a starting point for a structural model and was reproduced in FORTRAN, using a framework developed by Mader [33]. This FORTRAN beam model is verified in the subsequent section.

Another viable option explored during this thesis work is the equivalent plate model developed by Giles [11, 12, 13]. This model is suitable for the modelling of aircraft structures with a general planform such as cranked wing boxes — ideal for the BWB

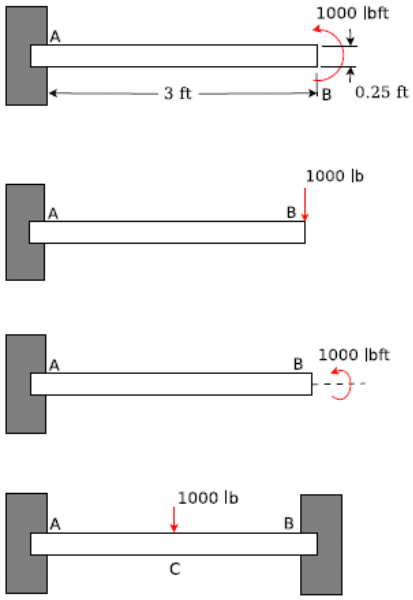

Figure A.1: Basic loading test cases [23].

configuration. The BWB configuration, in addition to a C-wing aircraft, is presented as an example application of this method in [13].

A.2.1 Beam Model Validation

For the theory behind the beam model formulation, the reader is referred to [23]. The following is a validation of the FORTRAN version, forBeam, of pyBeam [23] using the same test cases presented in [23]. Additional test cases and modification of the code to accommodate beams of varying cross-sections is recommended for future applications in order to more closely approximate a wing box with the beam element.

The first set of test cases are shown in Figure A.1. The results from forBeam are compared to theoretical results in Table A.1. The second test case is shown in Figure A.2. The original results of this test case were produced using ANSYS [23]. Table A.2 shows the results of forBeam compared to those from pyBeam and ANSYS. The results from forBeam and pyBeam are in agreement, with a consistent discrepancy between these results and those from ANSYS.

	Theoretical Results		forBeam Results	
Test Case	Slope[rad]	Deflection[ft]	Slope[rad]	Deflection[ft]
1 (at node B)	0.01054852	0.01582278	0.01054852	0.01582278
2 (at node B)	-0.01582278	-0.03164557	-0.01582278	-0.03164557
3 (at node B)	-0.01392946	-	-0.01392946	-
4 (at node C)	0	0.01582278	0	0.01582278

Table A.1: Comparison of theoretical and FORTRAN beam model (forBeam) results for Figure A.1 test cases.

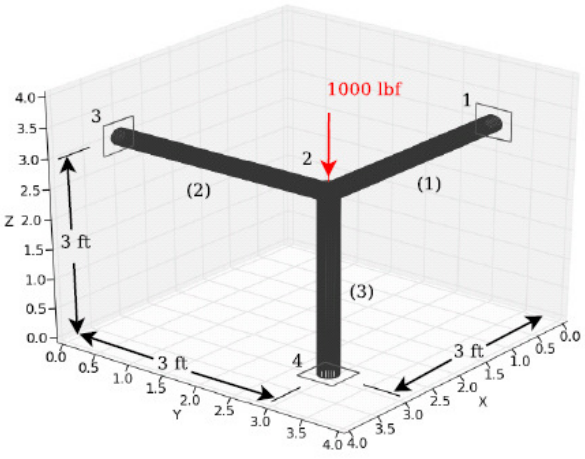

Figure A.2: Spatial frame test case [23].

	ANSYS	pyBeam	forBeam
Deflections/Slopes			
u_1 [ft]	9.9729e-08	9.9729e-08	9.9729e-08
u_2 [ft]	9.9729e-08	9.9729e-08	9.9729e-08
u_3 [ft]	-4.8668e-05	-4.8668e-05	-4.8668e-05
u_4 [rad]	-1.1138e-05	-1.1138e-05	-1.1138e-05
u_5 [rad]	1.1138e-05	1.1138e-05	1.1138e-05
u_6 [rad]	0.0	5.0825e-24	0.0
von Mises Stress [psft]			
Element 1	4700.3	4714.7	4714.7
Element 2	4700.3	4714.7	4714.7
Element 3	29543.0	29543.0	29543.0

Table A.2: Comparison of ANSYS, pyBeam and forBeam results for Node 2 [Figure A.2] deflections and element stress values.

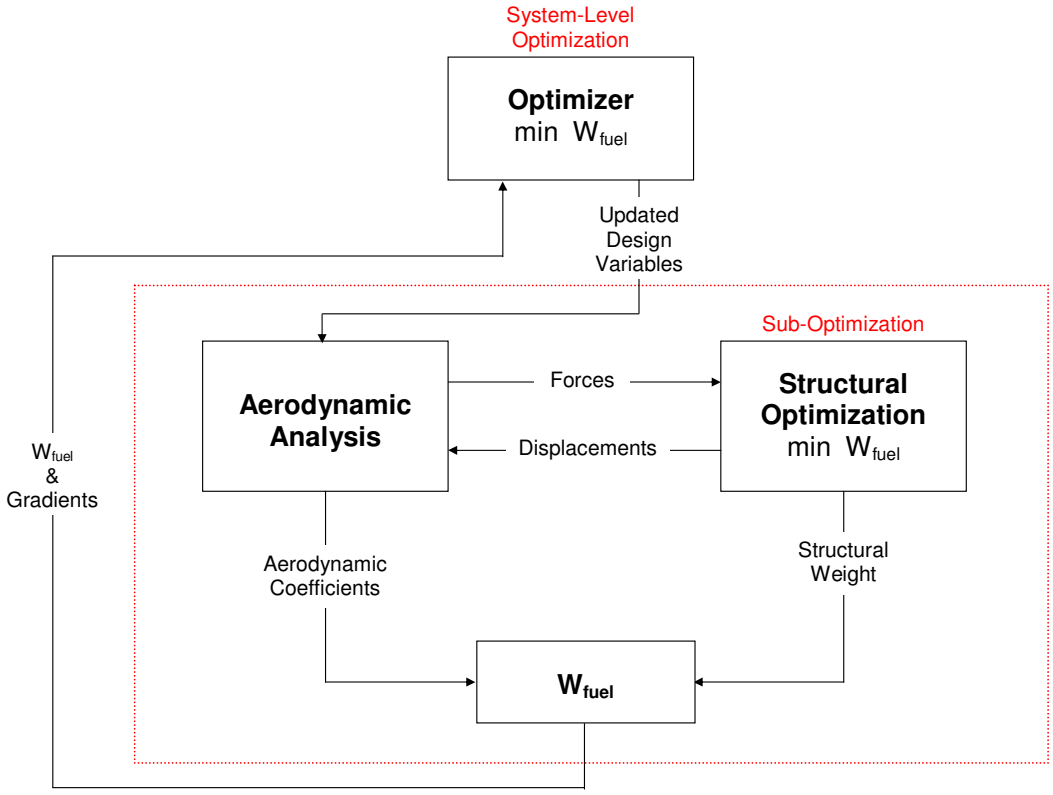

Figure A.3: Asymmetric suboptimization architecture.

A.3 Asymmetric Suboptimization Method Overview

In order to couple the aerodynamics and structural model, a subspace optimization method studied by Chittick and Martins [5, 6, 7] was considered. The following summarizes the idea behind this method, provides a brief description of the method in the context of its application to this project, and discusses the advantages and disadvantages. Other options are obviously available.

A.3.1 General Problem Definition

This section defines the optimization problem of incorporating structures with BWB aerodynamics with respect to this new method.

The idea behind the asymmetric suboptimization architecture is to solve a subspace optimization as part of an aerostructural analysis module. In a general system of N disciplines, each discipline can be classified as one of two types: analysis-only (N_a) or optimization-performing (N_o). In this case, there are two disciplines: aerodynamics (analysis-only) and structures (optimization-performing). In other words, each aerostructural iteration consists of an aerodynamic analysis and a structural sub-optimization. Overall, there are two optimizations: system-level optimization (coupled) and suboptimization (discipline specific). Figure A.3 illustrates these definitions. In this figure, note that the exchange of displacements between the two disciplines may be eliminated in the case where solely a weight value based on given aerodynamic forces is required, simplifying the optimization process slightly.

Notation: The three types of variables, x, y, and z, are defined below. The variables x and y exist for each discipline of concern.

x	local design variables	only affect one discipline
y	coupling variables	exchanged between disciplines
z	global or shared design variables	affect more than one discipline

The coupling variables for the ith discipline can be written as follows:
$y_i = y_i(x_i, y_j, z)$. Using similar notation for our case: $y_{aero} = y_{aero}(x_{aero}, y_{struct}, z)$.
The system-level optimization problem follows, where x_{a-i} and c_{a-i} are the local design variables and constraints of the i^{th} analysis-only discipline.:

$$\begin{aligned} \text{minimize} \quad & F(z, x, y) \\ \text{w.r.t.} \quad & z, x_{a-aero} \\ \text{s.t.} \quad & c_{a-aero}(z, x_{a-aero}, y_{aero}) \geq 0 \end{aligned}$$

The aerodynamics discipline must, of course, satisfy its governing equations, requiring the following to hold:

$$\begin{array}{rl} \text{given} & z, x_{a-aero}, y_{struct} \\ \text{solve} & \mathcal{R}_{aero}(z, x_{a-aero}, y_{struct}) = 0 \\ \text{to get} & y_{aero} \end{array}$$

The subspace optimization serves two purposes: solve the discipline's governing equations and perform an optimization using local design variables; here, x_{o-i} and c_{o-i} are the local design variables and constraints of the i^{th} optimization discipline:

$$\begin{array}{rl} \text{given} & z, y_{aero} \\ \text{minimize} & F(z, x, y) \\ \text{w.r.t.} & x_{o-struct} \\ \text{s.t.} & c_{o-struct}(z, x_{o-struct}, y_{struct}) \geq 0 \\ & \\ \text{with} & \mathcal{R}_{struct}(z, x_{o-struct}, y_{aero}) = 0 \\ \text{to get} & x_{o-struct}, y_{struct} \end{array}$$

A.3.2 Sensitivity Analysis: Coupled Post-Optimality Sensitivities

Considering the theory behind coupled-adjoint equations [37] and treating aerodynamics and the structural suboptimization as the two disciplines under consideration, the coupled-adjoint equations for this case are as follows.

$$\begin{bmatrix} \frac{\partial \boldsymbol{\mathcal{A}}}{\partial \boldsymbol{w}} & \frac{\partial \boldsymbol{\mathcal{A}}}{\partial \boldsymbol{y}} \\ \frac{\partial \boldsymbol{\mathcal{O}}}{\partial \boldsymbol{w}} & \frac{\partial \boldsymbol{\mathcal{O}}}{\partial \boldsymbol{y}} \end{bmatrix}^T \begin{bmatrix} \boldsymbol{\psi} \\ \boldsymbol{\zeta} \end{bmatrix} = - \begin{bmatrix} \frac{\partial F}{\partial \boldsymbol{w}}^T \\ \frac{\partial F}{\partial \boldsymbol{y}}^T \end{bmatrix}$$

where $\boldsymbol{\mathcal{A}}$ is the aerodynamic residual, $\boldsymbol{\mathcal{O}}$ is the structural suboptimization residual (defined below), $\boldsymbol{w}$ are the aerodynamic state variables, $\boldsymbol{y}$ are the structural suboptimization state variables, $\boldsymbol{\psi}$ is the flow adjoint vector, $\boldsymbol{\zeta}$ is the structural suboptimization adjoint vector, and F is the system-level objective function.

The total sensitivity with respect to the system-level design variables, $\boldsymbol{x}$, is written as

follows:

$$\frac{dF}{d\boldsymbol{x}} = \frac{\partial F}{\partial \boldsymbol{x}} + \boldsymbol{\psi}^T \frac{\partial \boldsymbol{\mathcal{A}}}{\partial \boldsymbol{x}} + \boldsymbol{\zeta}^T \frac{\partial \boldsymbol{\mathcal{O}}}{\partial \boldsymbol{x}}$$

Structural Sub-optimization Sensitivities

To define the structural suboptimization residuals, the suboptimization problem is first defined and can be summarized as follows:

$$\begin{aligned} \text{minimize} \quad & W_{fuel} \\ \text{w.r.t.} \quad & \boldsymbol{r} \\ \text{s.t.} \quad & \boldsymbol{\sigma} \leq \boldsymbol{\sigma}_{yield} \\ & \boldsymbol{r} \geq \boldsymbol{r}_{min} \end{aligned}$$

where W_{fuel} is the weight of the fuel, as based on the Breguet range equation, $\boldsymbol{r}$ and $\boldsymbol{r}_{min}$ are vectors of radii and minimum radii values, respectively, of the beam elements, and $\boldsymbol{\sigma}$ and $\boldsymbol{\sigma}_{yield}$ are the corresponding stress and yield stress values, respectively.

The structural residuals are given by:

$$\boldsymbol{K}\boldsymbol{u} - \boldsymbol{f} = \boldsymbol{0}$$

where $\boldsymbol{K}$ is the stiffness matrix, $\boldsymbol{u}$ the displacement vector, and $\boldsymbol{f}$ the force vector.

Combining this and the KKT conditions for the above suboptimization problem, the structural suboptimization residuals are obtained. The Lagrange multipliers for the stress and radius constraints are denoted by $\boldsymbol{\lambda}^T = [\boldsymbol{\lambda}_\sigma^T \quad \boldsymbol{\lambda}_r^T]$, the slack variables by $\boldsymbol{s}^T = [\boldsymbol{s}_\sigma^T \quad \boldsymbol{s}_r^T]$, and the state variables of the suboptimization by $\boldsymbol{y}^T = [\boldsymbol{u}^T \quad \boldsymbol{r}^T \quad \boldsymbol{s}^T \quad \boldsymbol{\lambda}^T]$.

$$\boldsymbol{\mathcal{O}} = \begin{cases} \boldsymbol{K}\boldsymbol{u} - \boldsymbol{f} = \boldsymbol{0} & \equiv \quad \boldsymbol{\mathcal{O}_S} \\ \frac{dW_{fuel}}{d\boldsymbol{r}} + \boldsymbol{\lambda}_\sigma^T \frac{d\boldsymbol{\sigma}}{d\boldsymbol{r}} - \boldsymbol{\lambda}_r^T \boldsymbol{I} = \boldsymbol{0} & \equiv \quad \boldsymbol{\mathcal{O}_\mathcal{L}} \\ \boldsymbol{\sigma}_{yield} - \boldsymbol{\sigma} - {\boldsymbol{s}_{\boldsymbol{\sigma}}}^2 = \boldsymbol{0} & \equiv \quad \boldsymbol{\mathcal{O}_\sigma} \\ \boldsymbol{r} - \boldsymbol{r}_{min} - {\boldsymbol{s}_{\boldsymbol{r}}}^2 = \boldsymbol{0} & \equiv \quad \boldsymbol{\mathcal{O}_r} \\ \boldsymbol{s}_\sigma \boldsymbol{\lambda}_\sigma = \boldsymbol{0}, \quad \boldsymbol{s}_r \boldsymbol{\lambda}_r = \boldsymbol{0} & \equiv \quad \boldsymbol{\mathcal{O}_{s\lambda}} \end{cases}$$

Partial derivative with respect to flow variables are :

$$\frac{\partial \boldsymbol{\mathcal{O}}}{\partial \boldsymbol{w}} = \begin{bmatrix} -\frac{\partial \boldsymbol{f}}{\partial \boldsymbol{w}} \\ \frac{\partial}{\partial \boldsymbol{w}}(\boldsymbol{\lambda}_\sigma^T \frac{d\boldsymbol{\sigma}}{d\boldsymbol{r}}) \\ \mathbf{0} \\ \mathbf{0} \\ \mathbf{0} \end{bmatrix}$$

Partial derivatives with respect to the suboptimization state variables are:

$$\frac{\partial \boldsymbol{\mathcal{O}}}{\partial \boldsymbol{y}} = \begin{bmatrix} \boldsymbol{K} & \frac{\partial \boldsymbol{K}}{\partial \boldsymbol{r}}\boldsymbol{u} & \mathbf{0} & \mathbf{0} \\ \mathbf{0} & \frac{\partial^2(W_{fuel})}{\partial \boldsymbol{r}^2} + \frac{\partial}{\partial \boldsymbol{r}}(\boldsymbol{\lambda}_\sigma^T \frac{d\boldsymbol{\sigma}}{d\boldsymbol{r}}) & \mathbf{0} & [\frac{d\boldsymbol{\sigma}}{d\boldsymbol{r}} \quad \boldsymbol{I}] \\ -\frac{\partial \boldsymbol{\sigma}}{\partial \boldsymbol{u}} & \mathbf{0} & [-2\boldsymbol{s}_\sigma \quad \mathbf{0}] & \mathbf{0} \\ \mathbf{0} & \boldsymbol{I} & [\mathbf{0} \quad -2\boldsymbol{s}_r] & \mathbf{0} \\ \mathbf{0} & \mathbf{0} & \boldsymbol{\lambda} & \boldsymbol{s} \end{bmatrix}$$

Partial derivatives with respect to the design variables are:

$$\frac{\partial \boldsymbol{\mathcal{O}}}{\partial \boldsymbol{x}} = \begin{bmatrix} \frac{\partial \boldsymbol{K}}{\partial \boldsymbol{x}}\boldsymbol{u} - \frac{\partial \boldsymbol{f}}{\partial \boldsymbol{x}} \\ \frac{\partial}{\partial \boldsymbol{x}}(\boldsymbol{\lambda}_\sigma^T \frac{d\boldsymbol{\sigma}}{d\boldsymbol{r}}) \\ -\frac{\partial \boldsymbol{\sigma}}{\partial \boldsymbol{x}} \\ \mathbf{0} \\ \mathbf{0} \end{bmatrix}$$

The above partial derivatives can be calculated using finite-differences or the complex-step approximation. For the higher-order derivatives, options discussed by Chittick [5] include a combination of finite-difference and complex-step evaluations, running two finite-difference routines, and the double application of automatic differentiation.

Aerodynamic Sensitivities

The flow Jacobian calculation ($\frac{\partial \boldsymbol{\mathcal{A}}}{\partial \boldsymbol{w}}$) is already in place [18]. The partial derivative with respect to the suboptimization state variables ($\frac{\partial \boldsymbol{\mathcal{A}}}{\partial \boldsymbol{y}}$) and the partial derivative with respect to the system-level design variables ($\frac{\partial \boldsymbol{\mathcal{A}}}{\partial \boldsymbol{x}}$) can be calculated using finite-differences.

Additional Considerations

Applicability and Advantages

Compared to a normal aerostructural optimization, this new architecture is found to be a more efficient approach under two conditions:

1. The number of MDA evaluations is adequately reduced by the simplified system-level optimization problem.

2. There exists a large enough discrepancy between the solution times of the disciplines under consideration.

Specifically, the new architecture is most effective when used for "an optimization that considers many constraint-critical design variables, and that involves a large aerodynamic-to-structural time ratio". As such, it is applicable in this case.

Disadvantages

The following are the key disadvantages of the new Coupled Post-Optimality Sensitivities (CPOS) method used for the sensitivity analysis of this new architecture:

- second-order sensitivity terms that appear in the structural suboptimization sensitivity equations;

- the adjoint CPOS equations cannot be solved if there is a singularity in the assembled matrix of partial derivatives of all the residuals with respect to all of the state variables;

- the Lagrange multipliers and slack variables of the optimized subproblems are required but may not be available, depending on the optimizer.

Appendix B

Multi-Point Optimization

Multi-point optimizations are of future interest not only for the BWB configuration but also for other aircraft configurations. Buckley and Zingg [3] as well as Zingg and Billing [79] have studied 2-dimensional single- and multi-point airfoil optimizations, including 18-point optimizations with dive and low-speed off-design points for a given aircraft. Three-dimensional multi-point optimizations have been studied using an unconstrained quasi-Newton optimizer [28]. The multi-point optimization functionality has also been implemented for use in conjunction with SNOPT as part of this thesis.

The goal of a multi-point optimization is to take into consideration multiple operating conditions more typically experienced by aircraft. A single-point optimization optimizes an aircraft for one specific operating condition, which does not guarantee acceptable performance at other design points of an aircraft. In contrast, a multi-point optimization is much more of a compromise between the various design points, resulting in an aircraft that performs well under a greater variety of conditions. These design points, as defined in [3], can be categorized into one of two types:

- On-design points: points at which we want to optimize and improve the aircraft performance (e.g. cruise conditions)
- Off-design points: points at which certain design constraints must be satisfied;

these are also effectively constraints on the on-design points since in order to meet them, the on-design point performance may be impacted (e.g. low-speed, high-C_L conditions).

In order to take these various conditions into consideration, the objective function for a multi-point optimization is a weighted function of each of the objective functions at each operating point considered:

$$\mathcal{J} = \sum_{i=1}^{N} w_i \mathcal{J}_i, \tag{B.1}$$

where $\mathcal{J}$ is the multipoint objective function, N is the total number of operating points, w_i is the weight for the ith operating point, and $\mathcal{J}_i$ is the ith objective function.

B.1 Verification and Implementation

In order to verify the implementation of the multi-point optimization, the inverse design test case presented in [18] was modified to a multi-point inverse design. This optimization test case is based on the surface pressure. For the given wing, this surface pressure is determined for an initial wing at each of the specified operating conditions to be used as part of the multi-point optimization. Control points on the initial wing are then perturbed. This perturbed wing serves as the starting point for the optimization. Given the objective function definition in [18], the modified multi-point variation is as follows:

$$\mathcal{J} = \sum_{i=1}^{N} w_i \left[\frac{1}{2} \sum_{j=1}^{N_{surf}} \left(p_j - p_{j,targ} \right)^2 \Delta A_j \right], \tag{B.2}$$

where w_i is the weight for operating point i, N is the total number of operating points, N_{surf} is the total number of surface nodes, ΔA_j is the surface area element at node j, p_j is the pressure at node j and $p_{j,targ}$, the target pressure at the same node. The surface area element is defined as the magnitude of the metric in the direction normal to the

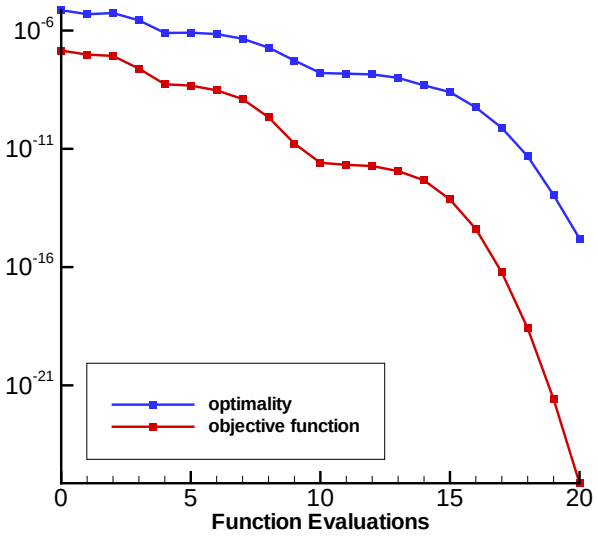

Figure B.1: Single-point inverse design with single perturbation.

surface at node j, multiplied by $\Delta\xi$ and $\Delta\eta$. Figure B.1 shows the results of a single-point case with a single perturbation, which converges as expected and came out identical to the results of code for which multi-point optimization was not implemented. Figure B.2 shows the results for a two-point inverse design with 6 perturbations. Specifically, all three degrees of freedom for 2 control points were perturbed. A different initial angle of attack was also specified for the second of the two points; the correct angle of attack was recovered. Mach numbers of 0.45 and 0.5 were used. Figure B.3 shows the results of a three-point inverse design for Mach 0.40, 0.45, 0.50 with 6 perturbations.

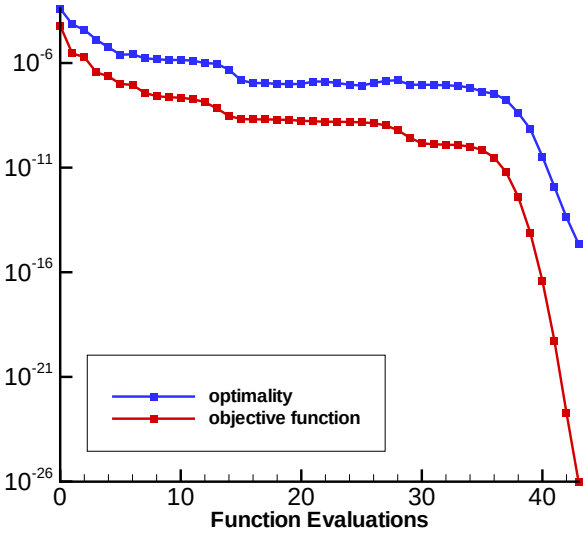

Figure B.2: Two-point inverse design with six perturbations and different initial angle of attack.

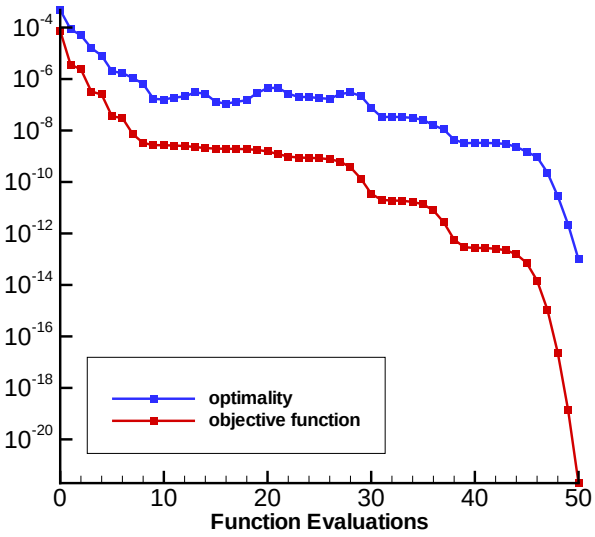

Figure B.3: Three-point inverse design with six perturbations.

Appendix C

Lift Constraint Definition

The lift coefficient is traditionally defined as follows:

$$C_L = \frac{L}{qS} = \frac{L}{\frac{1}{2}\rho V^2 S}, \tag{C.1}$$

where C_L is the lift coefficient, L is the lift (at cruise, equal to the weight of the aircraft) (N), q is the dynamic pressure (Pa), ρ is the freestream density (kg/m^3), V is the freestream velocity (m/s), and S is the selected reference area (m^2) — planform area, in this case.

As mentioned in Chapter 4, the target lift coefficient for the lift constraint is actually defined as $C_L S^*$, where S^* is the non-dimensionalized area.

To determine this value for a given design mission, we first rearrange Equation C.1 as follows,

$$C_L S = \frac{L}{q}. \tag{C.2}$$

Both sides now have dimensions of meters squared. Assuming the mesh geometry is non-dimensionalized by the reference root-chord length, this value needs to be non-dimensionalized. That is, the root-chord length on the mesh is of unit length, having been non-dimensionalized by the reference root-chord length.

The following relationship holds between the actual and non-dimensional areas:

$$S = S^* c^2, \tag{C.3}$$

where c is the reference root-chord length (m).

Substituting Equation C.3 into Equation C.2, we obtain the following:

$$C_L S^* c^2 = \frac{L}{q}, \tag{C.4}$$

which gives the non-dimensionalized form of the lift coefficient:

$$C_L S^* = \frac{L}{q c^2}. \tag{C.5}$$

In the case where the mesh geometry definition is based on the actual aircraft geometry values, $C_L S$ as defined in Equation C.2 should be used for the target lift coefficient. That is, rather than being of unit length, the root-chord length on the mesh would be equal to the reference root-chord length.

Note that lift coefficients quoted throughout the thesis are C_L, not $C_L S^*$.

References

[1] A. L. Bolsunovsky, N. P. Buzoverya, B. I. Gurevich, V. E. Denisov, A. I. Dunaevsky, L. M. Shkadov, O. V. Sonin, A. J. Udzhuhu, and J. P. Zhurihin, *Flying Wing - Problems and Decisions*, Aircraft Design, 4 (2001), pp. 193–219.

[2] K. Bradley, *A Sizing Methodology for the Conceptual Design of Blended-Wing-Body Transports*, tech. rep., NASA/CR-2004-213016, September 2004.

[3] H. P. Buckley, B. Y. Zhou, and D. W. Zingg, *Airfoil Optimization Using Practical Aerodynamic Requirements*, Journal of Aircraft, 47 (2010), pp. 1707–1719.

[4] O. Chernukhin, *Global Optimization Algorithms for Aerodynamic Design*, Master's thesis, University of Toronto Institute for Aerospace Studies, 2011.

[5] I. Chittick, *A New Subspace Optimization Method for Aerostructural Design*, Master's thesis, University of Toronto Institute for Aerospace Studies, 2007.

[6] I. R. Chittick and J. R. R. A. Martins, *Aero-Structural Optimization Using Adjoint Coupled Post-Optimality Sensitivities*, Structural and Multidisciplinary Optimization, 36 (2008), pp. 59–77.

[7] I. R. Chittick and J. R. R. A. Martins, *An Asymmetric Suboptimization Approach to Aerostructural Optimization*, Optimization and Engineering, 10 (2008), pp. 133 – 152.

[8] A. Diedrich, J. Hileman, D. Tan, K. Willcox, and Z. Spakovszky, *Multidisciplinary Design and Optimization of the Silent Aircraft*, in The 44th AIAA Aerospace Sciences Meeting and Exhibit, Reno, Nevada, United States, no. AIAA 2006-1323, January 2006.

[9] A. J. Diedrich, *The Multidisciplinary Design and Optimisation of an Unconventional, Extremely Quiet Transport Aircraft*, Master's thesis, Massachusetts Institute Of Technology, 2005.

[10] E. Galea, L. Filippidis, Z. Wang, and J. Ewer, *Fire and Evacuation Analysis in BWB Aircraft Configurations: Computer Simulations and Large-Scale Evacuation Experiment*, Aeronautical Journal, 114 (2010), pp. 271–277.

[11] G. L. Giles, *Equivalent Plate Analysis of Aircraft Wing Box Structures with General Planform Geometry*, Journal of Aircraft, 23, No. 11 (1986), pp. 859 – 864.

[12] ——, *Further Generalization of an Equivalent Plate Representation for Aircraft Structural Analysis*, Journal of Aircraft, 26, No. 1 (1989), pp. 67 – 74.

[13] ——, *Equivalent Plate Modeling for Conceptual Design of Aircraft Wing Structures*, in The 1st AIAA Aircraft Engineering Technology And Operations Congress, Los Angeles, CA, no. AIAA 95-3945, 1995.

[14] M. B. Giles and N. A. Pierce, *An Introduction to the Adjoint Approach to Design*, Flow, Turbulence and Combustion, 65 (2000), pp. 393–415.

[15] P. E. Gill, W. Murray, and M. A. Saunders, *SNOPT: An SQP Algorithm for Large-Scale Constrained Optimization*, SIAM Journal on Optimization, 12(4) (2002), pp. 979–1006.

[16] G. P. Guruswamy, *A Review of Numerical Fluids/Structures Interface Methods for Computations Using High-Fidelity Equations*, Computers and Structures, 80 (2002), pp. 31 – 41.

[17] M. D. Guynn, J. E. Freeh, and E. D. Olson, *Evaluation of a Hydrogen Fuel Cell Powered Blended-Wing-Body Aircraft Concept for Reduced Noise and Emissions*, tech. rep., NASA/TM-2004-212989, 2004.

[18] J. E. Hicken, *Efficient Algorithms for Future Aircraft Design: Contributions to Aerodynamic Shape Optimization*, PhD thesis, University of Toronto Institute for Aerospace Studies, 2009.

[19] J. E. Hicken and D. W. Zingg, *Parallel Newton-Krylov Solver for the Euler Equations Discretized Using Simultaneous-Approximation Terms*, AIAA Journal, 46 (2008), pp. 2773–2786.

[20] ——, *Aerodynamic Optimization Algorithm with Integrated Geometry Parameterization and Mesh Movement*, AIAA Journal, 48 (2010), pp. 400–413.

[21] ——, *Induced Drag Minimization of Nonplanar Geometries Based on the Euler Equations*, AIAA Journal, 48 (2010), pp. 2564–2575.

[22] IATA, *Jet Fuel Price Monitor*.
http : //www.iata.org/whatwedo/economics/fuel_monitor/Pages/index.aspx,
September 2010.

[23] P. W. Jansen, *Aerostructural Optimization of Non-Planar Lifting Surfaces*, Master's thesis, University of Toronto Institute for Aerospace Studies, 2009.

[24] G. K. W. Kenway, R. Henderson, J. E. Hicken, N. B. Kuntawala, D. W. Zingg, J. R. R. A. Martins, and R. G. McKeand, *Reducing Aviation's Environmental Impact Through Large Aircraft for Short Ranges*, in The 48th AIAA

Aerospace Sciences Meeting, Orlando, Florida, United States, no. AIAA 2010-1015, 2010.

[25] I. Kroo, *Innovations in Aeronautics*, in The 42nd AIAA Aerospace Sciences Meeting, January 5-8, 2004, Reno, NV, no. AIAA 2004-0001, 2004.

[26] ——, *Aircraft Design: Synthesis, and Analysis*, June 2010.

[27] D. S. Lee, D. W. Fahey, P. M. Forster, P. J. Newton, R. C. Wit, L. L. Lim, B. Owen, and R. Sausen, *Aviation and Global Climate Change in the 21st Century*, Atmospheric Environment, doi:10.1016/j.atmosenv.2009.04.024 (2009).

[28] T. M.-M. Leung, *A Newton-Krylov Approach to Aerodynamic Shape Optimization in Three Dimensions*, PhD thesis, University of Toronto Institute for Aerospace Studies, 2009.

[29] R. H. Liebeck, *Design of the Blended Wing Body Subsonic Transport*, Journal of Aircraft, 41(1) (2004), pp. 10–25.

[30] ——, *Blended Wing Body Design Challenges*, in The AIAA International Air and Space Symposium and Exposition: The Next 100 Years, Dayton, Ohio, no. AIAA 2003-2659, July 2003.

[31] R. H. Liebeck, M. A. Page, and B. K. Rawdon, *Blended-Wing-Body Subsonic Commercial Transport*, in The 36th Aerospace Sciences Meeting and Exhibit, Reno, Nevada, United States, no. AIAA 1998-0438, January 1998.

[32] Y. Lui, A. Dowling, H.-C. Shin, and A. Quayle, *Experimental Study of Surface Roughness Noise*, in The 13th AIAA/CEAS Aeroacoustics Conference (28th AIAA Aeroacoustics Conference), no. AIAA-2007-3449, 2007.

[33] C. Mader, *CIV1174: Finite Element Analysis Term Project - Wing Box Analysis using Bilinear Degenerate Shell Elements*, tech. rep., University of Toronto, 2009.

[34] R. Martínez-Val, E. Pérez, P. Alfaro, and J. Pérez, *Conceptual Design of a Medium Size Flying Wing*, Journal of Aerospace Engineering, 221 (2007), pp. 57–66.

[35] J. R. R. A. Martins, *AER1415: Optimization Concepts and Applications*. Course Notes.

[36] J. R. R. A. Martins, J. J. Alonso, and J. J. Reuther, *High-Fidelity Aerostructural Design Optimization of a Supersonic Business Jet*, Journal of Aircraft, 41 (2004), pp. 523–530.

[37] J. R. R. A. Martins, J. J. Alonso, and J. J. Reuther, *A Coupled-Adjoint Sensitivity Analysis Method for High-Fidelity Aero-Structural Design*, Optimization and Engineering, 6 (2005), pp. 33 – 62.

[38] M. Meheut, R. Grenon, G. Carrier, M. Defos, and M. Duffau, *Aerodynamic Design of Transonic Flying Wing Configurations*, in KATnet II: Conference on "Key Aerodynamic Technologies", Bremen, Germany, 12-14th May 2009, 2009.

[39] B. Mialon and M. Hepperle, *Flying Wing Aerodynamics Studies at ONERA and DLR*, in CEAS/KATnet Conference on Key Aerodynamic Technologies, http://www.onera.fr/daap/ailes-volantes/flying-wing-aerodynamics-Onera-DLR.pdf, April 2005.

[40] A. Morris, P. Arendsen, G. LaRocca, M. Laban, R. Voss, and H. Hönlinger, *MOB - A European Project on Multidisciplinary Design Optimisation*, in The 24th International Congress of the Aeronautical Sciences, 2004.

[41] V. Mukhopadhyay, *Blended-Wing-Body (BWB) Fuselage Structural Design for Weight Reduction*, in The 46th AIAA/ASME/ASCE/AHS/ASC Structures, Structural Dynamics, and Materials Conference, no. AIAA 2005-2349, 2005.

[42] V. Mukhopadhyay, J. Sobieszczanski-Sobieski, I. Kosaka, G. Quinn, and G. Vanderplaats, *Analysis, Design, and Optimization of Noncylindrical Fuselage for Blended-Wing-Body Vehicle*, Journal Of Aircraft, 41 (2004), pp. 925–930.

[43] National Geographic, *Hitler's Stealth Fighter*. Documentary, June 2009.

[44] M. Nemec and D. W. Zingg, *A Newton-Krylov Algorithm for Aerodynamic Design Using the Navier-Stokes Equations*, AIAA Journal, 40 (2002), pp. 1146 – 1154.

[45] J. Nocedal and S. J. Wright, *Numerical Optimization*, Springer-Verlag New York, Inc., 1999.

[46] C. Österheld, W. Heinze, and P. Horst, *Preliminary Design of a Blended Wing Body Configuration Using the Design Tool PrADO*, in The Proceedings of the CEAS Conference on Multidisciplinary Aircraft Design and Optimisation, Cologne, June 2001.

[47] T. E. Pambagjo, K. Nakahashi, S. Obayashi, and K. Matsushima, *An Alternate Configuration for a Regional Transport Airplane*, Transactions of the Japan Society for Aeronautical and Space Sciences, 45(148) (2002), pp. 94–101.

[48] ——, *Aerodynamic Design of a Medium Size Blended-Wing-Body Airplane*, in The 39th AIAA Aerospace Sciences Meeting and Exhibit, Reno, Nevada, United States, no. AIAA 2001-129, January 2001.

[49] PBS/Kontent Real Production, e^2 *Series*. Webcast, February 2008.

[50] S. Peigin and B. Epstein, *Computational Fluid Dynamics Driven Optimization of Blended Wing Body Aircraft*, AIAA Journal, 44(11) (2006), pp. 2736–2745.

[51] A. P. Plas, V. Madani, M. A. Sargeant, E. M. Greitzer, C. A. Hall, and T. P. Hynes, *Performance of a Boundary Layer Ingesting (BLI) Propulsion*

System, in The 45th Aerospace Sciences Meeting and Exhibit Conference, Reno, Nevada, no. AIAA-2007-0450, 2007.

[52] M. A. Potsdam, M. A. Page, and R. H. Liebeck, *Blended Wing Body Analysis and Design*, in The 15th AIAA Applied Aerodynamics Conference, Atlanta, Georgia, no. AIAA 1997-2317, June 1997.

[53] N. Qin, A. Vavalle, A. LeMoigne, M. Laban, K. Hackett, and P. Weinerfelt, *Aerodynamic Considerations of Blended Wing Body Aircraft*, Progress in Aerospace Sciences, 40 (2004), pp. 321–343.

[54] N. Qin, A. Vavalle, and A. L. Moigne, *Spanwise Lift Distribution for Blended Wing Body Aircraft*, Journal of Aircraft, 42 (2005), pp. 356–365.

[55] N. Qin, A. Vavalle, A. L. Moigne, M. Laban, K. Hackett, and P. Weinerfelt, *Aerodynamic Studies for Blended Wing Body Aircraft*, in The 9th AIAA/ISSMO Symposium on Multidisciplinary Analysis and Optimization, no. AIAA 2002-5448, 2002.

[56] A. Quayle, A. Dowling, H. Babinsky, W. Graham, H. Shin, and P. Sijtsma, *Landing Gear for a Silent Aircraft*, in The 45th AIAA Aerospace Sciences Meeting and Exhibit, Reno, Nevada, no. AIAA-2007-231, 2007.

[57] D. Raymer, *Aircraft Design - A Conceptual Approach, Fourth Edition*, AIAA Education Series, 2006.

[58] H. J. D. Reynolds, T. G. Reynolds, and R. J. Hansman, *Human Factors Implications of Continuous Descent Approach Procedures for Noise Abatement*, Air Traffic Control Quarterly, 14, No. 1 (2006), pp. 25–45.

[59] D. Roman, J. B. Allen, and R. H. Liebeck, *Aerodynamic Design Challenges of the Blended-Wing-Body Subsonic Commercial Transport*, in The 18th AIAA Applied

Aerodynamics Conference, Denver, Colorado, United States, no. AIAA-2000-4335, August 2000.

[60] D. Roman, R. Gilmore, and S. Wakayama, *Aerodynamics of High-Subsonic Blended-Wing-Body Configurations*, in The 41st Aerospace Sciences Meeting and Exhibit, Reno, Nevada, United States, no. AIAA 2003-554, January 2003.

[61] D. J. Roskam, *Airplane Design - Part V: Component Weight Estimation*, Roskam Aviation and Engineering Corporation, 1989.

[62] M. A. Sargeant, T. P. Hynes, W. R. Graham, J. I. Hileman, M. Drela, and Z. S. Spakovsky, *Stability of Hybrid-Wing-Body-Type Aircraft with Centerbody Leading-Edge Carving*, Journal Of Aircraft, 47 (2010), pp. 970–974.

[63] S. Siouris and N. Qin, *Study of the Effects of Wing Sweep on the Aerodynamic Performance of a Blended Wing Body Aircraft*, Journal of Aerospace Engineering, 221(1) (2007), pp. 47–55.

[64] J. Sobieszczanski-Sobieski and R. T. Haftka, *Multidisciplinary Aerospace Design Optimization: Survey of Recent Developments*, Structural And Multidisciplinary Optimization, Volume 14, Number 1, DOI: 10.1007/BF01197554 (1997), pp. 1–23.

[65] N. Stern, *The Stern Review on the Economics of Climate Change*, Cambridge University Press, 2007, 2007.

[66] M. Stettner and R. Voss, *Aeroelastics, Flight Mechanics and Handling Qualities of the MOB BWB Configuration*, in The 9th AIAA/ISSMO Symposium on Multidisciplinary Analysis and Optimization, no. AIAA 2002-5449, 2002.

[67] H. Strüber and M. Hepperle, *Aerodynamic Optimisation of a Flying Wing Transport Aircraft*, New Results in Numerical and Experimental Fluid Mechanics V, 92 (2006), pp. 69–76.

[68] The Boeing Company, *Long-Term Market: Current Market Outlook 2010 - 2029*, September 2010.

[69] The Cambridge-MIT Institute, *The Silent Aircraft Initiative*. http://silentaircraft.org/, 2006.

[70] E. Torenbeek, *Synthesis of Subsonic Airplane Design*, Delft University Press, 1982.

[71] A. H. Truong, C. A. Oldfield, and D. W. Zingg, *Mesh Movement for a Discrete-Adjoint Newton-Krylov Algorithm for Aerodynamic Optimization*, AIAA Journal, 46 (2008), pp. 1695 –1704.

[72] UIUC Applied Aerodynamics Group, *UIUC Airfoil Coordinates Database*, 2010.

[73] A. Velicki, P. Thrash, and D. Jegley, *Airframe Development for the Hybrid Wing Body Aircraft*, in The 47th AIAA Aerospace Sciences Meeting Including The New Horizons Forum and Aerospace Exposition, no. AIAA 2009-932, January 2009.

[74] D. D. Vicroy, *Blended-Wing-Body Low-Speed Flight Dynamics: Summary of Ground Tests and Sample Results*, in The 47th AIAA Aerospace Sciences Meeting Including The New Horizons Forum And Aerospace Exposition, no. AIAA 2009-933, January 2009.

[75] S. Wakayama, *Blended-Wing-Body Optimization Problem Setup*, in The 8th AIAA/USAF/NASA/ISSMO Symposium on Multidisciplinary Analysis and Optimization, Long Beach, CA, no. AIAA 2000-4740, September 2000.

[76] S. Wakayama and I. Kroo, *The Challenge and Promise of Blended-Wing-Body Optimization*, in The 7th AIAA/USAF/NASA/ISSMO Symposium on Multidisciplinary Analysis and Optimization, St. Louis, MO, no. AIAA 1998-4736, September 1998.

[77] G. Walker and S. D. King, *The Hot Topic: What We Can Do About Global Warming*, Greystone Books, 2008.

[78] W. Wong, A. LeMoigne, and N. Qin, *Parallel Adjoint-Based Optimisation of a Blended Wing Body Aircraft with Shock Control Bumps*, The Aeronautical Journal, 111, No. 1117 (2006), pp. 165 – 174.

[79] D. W. Zingg and L. Billing, *Toward Practical Aerodynamic Design Through Numerical Optimization*, in The 18th AIAA Computational Fluid Dynamics Conference, Miami, FL, no. AIAA 2007-3950, June 2007.